FLAML version 2.3.3 model-based assessment of gross primary productivity at forest, grassland, and cropland ecosystem sites

Jie Lai [a, b], Yuan Zhang [a], Anzhi Wang [a], Wenli Fei [a], Yiwei Diao [c], Rongping Li [d], Jiabin Wu [a, *]

[a] CAS Key Laboratory of Forest Ecology and Silviculture, Institute of Applied Ecology, Chinese Academy of Sciences, Shenyang 110016, China
[b] University of Chinese Academy of Sciences, Beijing 101408, China
[c] Key Laboratory of Ecosystem Carbon Source and Sink, China Meteorological Administration (ECSS-CMA), Wuxi University, Wuxi, 214105, China
[d] Institute of Atmospheric Environment, China Meteorological Administration, Shenyang 110016, China
* Correspondence: wujb@iae.ac.cn

Abstract

Accurately estimating Gross Primary Productivity (GPP) in terrestrial ecosystems is essential for understanding the global carbon cycle. Satellite-based Light Use Efficiency (LUE) models are commonly employed for simulating GPP. However, the variables and algorithms related to environmental limiting factors differ significantly across various LUE models, leading to high uncertainty in GPP estimation. In this work, we developed a series of FLAML-LUE models with different variable combinations. These models utilize the Fast Lightweight Automated Machine Learning (FLAML) framework, using variables of LUE models, to investigate the potential of estimating site-scale GPP. Incorporating meteorological data, eddy covariance measurements, and remote sensing indices, we employed FLAML-LUE models to assess the impact of various variable combinations on GPP across different temporal scales, including daily, 8-day, 16-day, and monthly intervals. Cross-validation analyses indicated that the FLAML-LUE model performs excellently in GPP prediction, accurately simulating

both its temporal variations and magnitude, particularly in mixed forests and coniferous

forests, with average R^2 values for daily-scale simulations reaching 0.92 and 0.91,

respectively. However, the model performed less effectively in alpine shrubland and

typical grassland ecosystems, though it still outperformed both MODIS GPP and PML

GPP in terms of performance. Furthermore, the model's adaptability under extreme

climate conditions was evaluated, and the results showed that high temperatures and

high VPD lead to a slight decrease in model accuracy, though R^2 remains around 0.8.

Under drought conditions, the model's performance improved slightly in croplands and

evergreen broadleaf forests, although it declined at some sites. This study offers an

approach to estimate GPP fluxes and evaluate the impact of variables on GPP estimation.

It has the potential to be applied in predicting GPP for different vegetation types at a

regional scale.

Keywords: Light Use Efficiency; Gross Primary Productivity; Automated Machine

Learning; Fast Lightweight Automated Machine Learning

1. Introduction

The global carbon budget mainly addresses the carbon reserves in the atmosphere,

oceans, and terrestrial (Barbour, 2021), with terrestrial ecosystems being vital for

regulating the global carbon cycle (Gherardi and Sala, 2020; Landry and Matthews,

2016). Terrestrial ecosystems primarily absorb atmospheric carbon dioxide through the

process of plant photosynthesis, which is crucial for regulating climate and mitigating

global warming (Sellers et al., 2018; Beer et al., 2010; Cox et al., 2000). Gross primary

productivity (GPP) is a critical measure of carbon exchange between terrestrial

ecosystems and the atmosphere (Menefee et al., 2023). Accurate quantification of GPP

is essential for evaluating carbon balance and comprehending the response of terrestrial

ecosystems to climate change (Sellers et al., 2018).

The primary method currently used for measuring CO_2 exchange between

ecosystems and the atmosphere is the eddy covariance technique (Chen et al., 2020; Yu

et al., 2016). This technique precisely measures Net Ecosystem Exchange (NEE), which

is the difference between the carbon released by ecosystem respiration (ER) and the

carbon taken up by photosynthesis (Bhattacharyya et al., 2013). While flux observation

sites based on the eddy covariance (EC) technique can dynamically monitor site-scale

carbon fluxes, expanding their findings to larger regional scales remains challenging,

mainly due to the sparse and spatially non-uniform distribution of flux sites (Xie et al.,

2023; Jung et al., 2020). Remote sensing data is widely used in ecosystem carbon cycle

research as it can provide information on the spatial dynamics of vegetation and climate

at a larger scale (Xiao et al., 2019). By extrapolating spatially using models that

incorporate remote sensing and climate data, it is possible to estimate global GPP based

on observations of GPP at the site level. Therefore, remote sensing has become a crucial

data resource for estimating GPP (Cai et al., 2021; Xiao et al., 2019; Wang et al., 2011).

Light Use Efficiency (LUE) models based on satellite observations are commonly

employed to simulate GPP (Zhang et al., 2023; Zhang et al., 2015; Jiang et al., 2014).

Such models include Physiological Principles Predicting Growth using Satellite data

(3-PGS, Coops and Waring, 2001), the Carnegie-Ames- Stanford Approach Model

(CASA, Potter et al., 1993), the Eddy Covariance–Light Use Efficiency Model (EC-

LUE, Yuan et al., 2010, 2007), the MODIS Global Terrestrial Gross and Net Primary Production (MOD17, Running et al., 2004), the Vegetation Photosynthesis Model (VPM, Xiao et al., 2003), and the Vegetation Photosynthesis and Respiration Model (VPRM, Mahadevan et al., 2008). Among all the forecasting methods (Coops and Waring, 2001; Potter et al., 1993), the LUE model is widely utilized for simulating the spatio-temporal dynamics of GPP due to its simplicity and strong theoretical foundation. Over the past few decades, numerous GPP models utilizing LUE have been developed (Pei et al., 2022).

Despite significant advances in LUE theory for GPP estimation, uncertainties persist in GPP models utilizing LUE. Firstly, differences in environmental limiting factors among various LUE models contribute significantly to the uncertainty in GPP estimation. For example, Cai et al. (2014) found a strong positive correlation between water effectiveness and GPP estimate factors, while other studies found that the LUE model estimates of GPP were strongly correlated with the vegetation index, which affects the photosynthetic capacity of vegetation through leaf nitrogen content (Peltoniemi et al., 2012; Ercoli, 1993).

Recently, with the massive accumulation of satellite data and ground-based observations, more and more studies have applied machine learning (ML) methods to model ecosystem processes (Zhao et al., 2019; Alemohammad et al., 2017; Chaney et al., 2016). ML is a modeling solution that differs from simple regression models and complex simulation models in its approach. It is very effective in handling large-scale multivariate data with complex relationships between predictors (Reichstein et al., 2019;

94   Tramontana et al., 2016). These data-driven models are particularly suited for capturing

95   nonlinear ecosystem dynamics but often require large training datasets and may lack

96   explicit links to real-world processes. However, their ability to uncover spatial patterns

97   without process-based constraints makes them valuable for spatial predictions.

98   Consequently, ML-based approaches have gained popularity in recent years. For

99   example, Kong et al. (2023) developed a hybrid model that combines ML and LUE

100   model to estimate GPP. This hybrid model improves the LUE model by integrating a

101   machine learning approach (MLP, multi-layer perceptron), and estimates GPP using the

102   MLP-based LUE framework along with additional required inputs. Chang et al. (2023)

103   constructed RFR-LUE models that utilize the Random Forest Regression (RFR)

104   algorithm with variables of LUE models to assess the potential of site-scale GPP

105   estimation.

106   Lately, Automated Machine Learning (AutoML) has demonstrated significant

107   potential in constructing data-driven models automatically (Zheng et al., 2023).

108   Numerous sophisticated open-source AutoML frameworks have been suggested by

109   computer scientists, including Automated WEKA (Auto-WEKA, Thornton et al., 2013),

110   H2O AutoML (H2O, LeDell and Poirier, 2020), Tree-based Pipeline Optimization Tool

111   (TPOT, Melanie, 2023), Automated Machine Learning with Gluon (AutoGluon,

112   Erickson et al., 2020), Fast Lightweight Automated Machine Learning (FLAML, Wang

113   et al., 2021), and AutoKeras (Rosebrock, 2019). These frameworks are extensively used

114   in finance, manufacturing, healthcare, and mobile communications, among other fields

115   (Adams et al., 2020), with FLAML being particularly favored for its efficiency in rapid

prototyping and deployment in research and production settings. FLAML is a powerful

framework for AutoML, known for its speed in identifying top-performing models and

optimal hyperparameters through parallel optimization and smart search algorithms.

FLAML integrates several effective search strategies, outperforming other leading

AutoML libraries on large benchmarks even with constrained budgets (Wang et al.,

2021).

In this research, a new model called FLAML-LUE was created by combining

FLAML model with LUE-based models, the latter provides the key variables of

vegetation growth for modeling. Such knowledge-and-data-driven models aim to

reduce the large uncertainty in estimating GPP. The specific objectives of this study are:

(1) to evaluate the overall performance of models using different input variables,

including the fraction of photosynthetically active radiation absorbed by vegetation

(fPAR) and various water stress indicators, across multiple sites and vegetation types

based on eddy covariance observations; (2) to assess model performance under extreme

climatic conditions, such as high temperature, elevated vapor pressure deficit (VPD),

and drought.

2. Materials and methods

2.1 Site description

Figure 1 displays the geographical locations of the 20 flux sites selected for the

study. These sites are situated in various climatic zones and ecosystem types including

forest, grassland, and cropland. The observation data for these sites comes from the

Science Data Bank (SDB, https://www.scidb.cn/en/). Detailed information about the

138   sites is provided in **Table 1**.

139
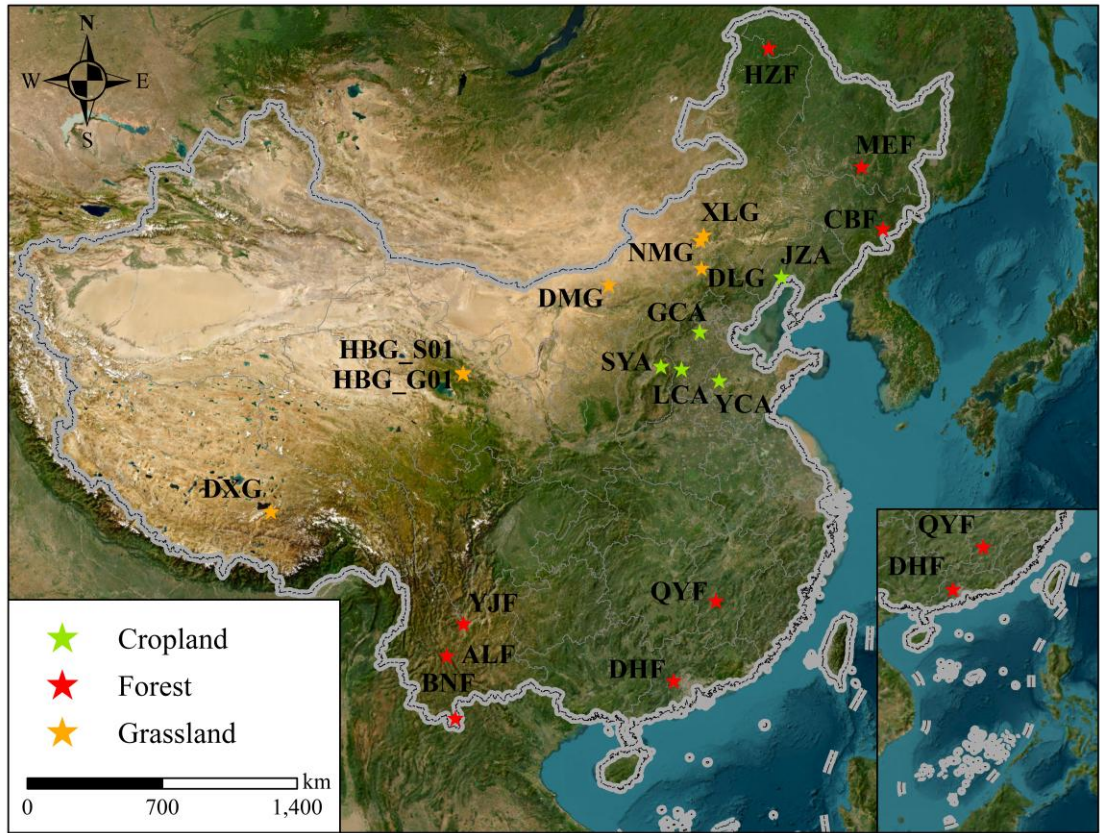
140   **Figure 1.** The location map of the flux site is based on the map approved by the National Surveying
141   and Mapping Bureau of China (Approval No. GS (2019)1822). The topographic map is derived
142   from data provided by Esri, Maxar, Earthstar Geographics, and the GIS User Community (Service
143   Layer Credits).

144   **Table 1**

145   Basic information on the 20 flux stations.

Site	Longitude (°E)	Latitude (°N)	Ecosystem type	Time Range	Classified
HZF	123.018	51.781	Forest	2014-2018	NF
MEF	127.668	45.417	Forest	2016-2018	DBF
CBF	128.096	42.403	Forest	2003-2010	MF
QYF	115.058	26.741	Forest	2003-2010	NF
ALF	101.028	24.541	Forest	2009-2013	EBF
DHF	112.534	23.173	Forest	2003-2010	MF
BNF	101.577	21.614	Forest	2003-2015	EBF
YJF	101.827	26.080	Forest	2013-2015	SAV
XLG	116.671	43.554	Grassland	2006-2014	GRA
NMG	116.404	43.326	Grassland	2003-2010	Grassland
DLG	116.284	42.047	Grassland	2006-2015	Grassland
DMG	110.328	41.644	Grassland	2015-2018	Grassland

HBG_G01	101.313	37.613	Grassland	2015-2020	MEA
HBG_S01	101.331	37.665	Grassland	2003-2013	SHR
DXG	91.066	30.497	Grassland	2003-2010	MEA
JZA	121.202	41.148	Cropland	2005-2014	SC
GCA	115.735	39.149	Cropland	2020-2022	DC
SYA	113.200	37.750	Cropland	2012-2014	SC
LCA	114.413	37.531	Cropland	2013-2017	DC
YCA	116.570	36.829	Cropland	2003-2010	DC

Note: Vegetation types in the table are classified based on the land cover characteristics of each flux site and are used in subsequent model simulations. NF: Needle-leaved Forest; DBF: Deciduous Broadleaved Forest; MF: Mixed Forest; EBF: Evergreen Broadleaved Forest; SAV: Savannas; GRA: Typical Grassland; MEA: Alpine Meadow; SHR: Shrubs; SC: Single Cropping; DC: Double Cropping.

2.2 Data

2.2.1 Eddy covariance data

EC data were collected at 20 sites, including 8 forests sites, 7 grasslands sites, and 5 cropland sites (**Table 1**). Flux and meteorological data were collected every half hour from the mentioned sites. The flux and meteorological data underwent standardized quality control and corrections, ensuring high reliability and making them suitable for validating various GPP models and remote sensing observations. However, ER data were missing at some sites (DLG, LCA, XLG). To address this, the Lloyd & Taylor equation (Reichstein et al., 2005; Lloyd and Taylor, 1994) was applied to estimate ER based on nocturnal respiration data. Daytime and nighttime periods were distinguished using shortwave radiation (Rg), with a threshold of 10 W/m². The temperature–response relationship derived from nighttime ER was extrapolated to estimate daytime ER. This is a commonly used method for processing flux data at flux tower sites.

$$R_{eco} = R_{eco.ref} \exp\left(E_0\left(\frac{1}{T_{ref}-T_0} - \frac{1}{T_{air}-T_0}\right)\right) \tag{1}$$

$$GPP = ER - NEE \tag{2}$$

164   In equation (1), R_{eco} is the nocturnal ecosystem respiration value, $R_{eco.ref}$ is the ER value

165   at the reference temperature, T_{ref} is the reference temperature (298.16K), E_0 is constant

166   (308.56K), T_0 is the minimum temperature at which respiration stops, set at 227.13K,

167   and T_{air} is the air temperature or soil temperature (K). Daytime GPP was then estimated

168   by subtracting NEE from the total daytime ER.

2.2.2 MODIS data

170   In this study, remote sensing data were primarily obtained from the Moderate

171   Resolution Imaging Spectroradiometer (MODIS). MODIS data offer a spatial

172   resolution of 500 meters and an 8-day temporal resolution. These datasets were sourced

173   from the Google Earth Engine (GEE) platform (Gorelick et al., 2017). To align with the

174   spatial and temporal scales of flux tower observations and reduce the impact of missing

175   data (Schmid, 2002), we applied the Savitzky-Golay smoothing filter with a window

176   size of 10 to process the vegetation indices. Vegetation and water indices derived from

177   MODIS data included the enhanced vegetation index (EVI), normalized difference

178   vegetation index (NDVI), and land surface water index (LSWI), which were calculated

179   using the formulas presented in **Table 2**.

2.2.3 ERA5-LAND

181   ERA5-Land (Hersbach et al., 2020) is a global high-resolution reanalysis dataset

182   produced by the European Centre for Medium-Range Weather Forecasts (ECMWF)

183   under the Copernicus Climate Change Service (C3S). It provides hourly land surface

184   variables at a spatial resolution of 0.1°, generated using a dedicated land surface model

185   driven by the ERA5 climate reanalysis. The dataset integrates advanced land surface

186 modeling and data assimilation techniques, offering a wide range of variables such as

187 air temperature, soil moisture, precipitation, and snow depth. In this study, site-specific

188 variables including air temperature (T), soil water content (SW), precipitation (Pre),

189 and leaf area index (LAI) were extracted from ERA5-Land. In addition,

190 photosynthetically active radiation (PAR), evapotranspiration fraction (EF), VPD and

191 relative humidity (RH) were calculated and derived from available ERA5-Land

192 variables using GEE.

2.2.4 SPEI Database, Version 2.10

194 The SPEI Database, Version 2.10 (Vicente-Serrano et al., 2010) provides global

195 data of the Standardized Precipitation-Evapotranspiration Index (SPEI) across temporal

196 scales from 1 to 48 months. Developed by the Climatic Research Unit (CRU), this

197 dataset combines precipitation and potential evapotranspiration (PET) to assess drought

198 conditions. Negative SPEI values indicate drought, while positive values signify wet

199 periods. In this study, SPEI values less than -1.5 were used to identify drought months

200 at each flux station, highlighting significant moisture deficits that affect vegetation

201 growth and ecosystem productivity (Qian et al., 2024).

2.3 Model Construction

203 Most LUE models typically incorporate four main groups of variables: PAR, fPAR,

204 temperature, and water-related stress indicators. In previous studies, vegetation indices

205 such as EVI, NDVI, or LAI have been widely used as proxies for fPAR, representing

206 the fraction of PAR absorbed by the plant canopy (Chang et al., 2023; Qian et al., 2024).

207 In this study, we selected six water-related indicators based on their ecological

208 relevance: plant-based indicators (LSWI and EF), soil-based indicators (SW), and

209 atmospheric indicators (VPD, precipitation, and relative humidity). Previous research

210 has shown that plant-based indicators like LSWI and EF effectively capture canopy-

211 level drought stress (Anderson et al., 2007; Xiao et al., 2004). Soil moisture regulates

212 water availability at the root level, which strongly influences photosynthetic activity,

213 particularly under water-limited conditions (Vicca et al., 2014; Reichstein et al., 2007).

214 Meanwhile, atmospheric indicators such as VPD, precipitation, and RH influence

215 stomatal conductance and transpiration by altering the vapor pressure gradient between

216 the leaf surface and the surrounding air (Wang et al., 2018; Novick et al., 2016). To

217 assess the relative importance of these different types of water stress indicators in

218 estimating GPP, we developed machine learning models using each group individually.

219 This allowed us to identify the most effective type of water-related variable for

220 simulating GPP across diverse ecosystems within the LUE modeling framework.

221   The flowchart of this study is shown in **Figure 2**.
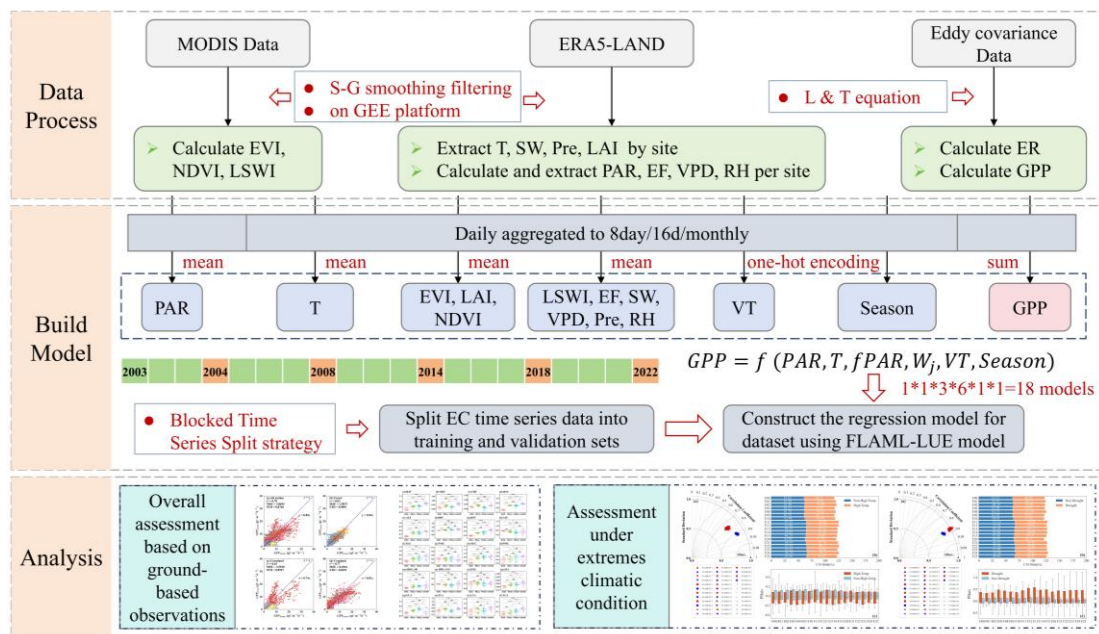
222

2.3.1 Data pre-processing and splitting strategy

The primary datasets for estimating GPP with FLAML-LUE models include multi-year continuous EC flux data, satellite-based observations, and ERA5-Land climate reanalysis data. Prior research (Jung et al., 2011) has demonstrated notable seasonal fluctuations in GPP, we divided the time series data into four distinct seasons. Moreover, the vegetation cover type, which varies across different ecosystems, greatly impacts the accuracy of GPP simulation (Chang et al., 2023). Hence, we integrate vegetation type as a factor in our model.

The pre-processed dataset was divided into training and testing sets using the Blocked Time Series Split strategy. Given the temporal dependency of the data, standard cross-validation is not suitable for time series analysis (Reichstein et al., 2019). Instead, a block-based and non-continuous split is applied to preserve the temporal structure. In this approach, the time series is partitioned into several non-overlapping continuous training blocks (e.g., 2003-2005, 2007-2009, 2011-2013, 2015-2017, 2019-2021), with independent years reserved as the validation set following each training block (e.g., 2006, 2010, 2014, 2018, 2022). This strategy ensures that the temporal order is maintained, preventing future data from leaking into the training process and thus avoiding invalid predictions. Additionally, the method incorporates validation over multiple periods, enabling the assessment of model generalization across different climate conditions, which is crucial for evaluating the model's robustness under varying environmental scenarios.

Table 2

Predictor variables for driving the FLAML models and their specifications.

	Variable	Acquired method (formula)	Original Spatial Resolution	Data Source
fPAR	EVI	$2.5 \times (R_{nir} - R_{red}) / (R_{nir} + 6.0 \times R_{red} - 7.5 \times R_{blue} + 1)$	500m	MOD09GA
	NDVI	$(R_{nir} - R_{red}) / (R_{nir} + R_{red})$		
	LAI	-	~10km	ERA5-Land
Water	LSWI	$(R_{nir} - R_{swir}) / (R_{nir} + R_{swir})$	500m	MOD09GA
	EF (%)	$EF = LE/(LE+H)$	~10km	ERA5-Land
	SW (m³/ m³)	-	~10km	ERA5-Land
	VPD	$VPD = e_s - e$ $e = 6.112 \times \exp((17.67 \times T_d) + (243.5 + T_d))$ $e_s = 6.112 \times \exp((17.67 \times T) + (243.5 + T))$	~10km	ERA5-Land
	Pre (mm)	-	~10km	ERA5-Land
	RH (%)	$RH = (e/e_s) \times 100$	~10km	ERA5-Land
Radiation	PAR(μ mol m⁻² s⁻¹)	-	~10km	ERA5-Land
Temperature	T (℃)	-	~10km	ERA5-Land
VT	EBF, DBF, NF, MF, GRA, MEA, SHR, SC, DC	One-hot encoding	invariant	-
Season	Spring, Summer, Autumn, Winter	One-hot encoding	invariant	-

Note: EVI: Enhanced Vegetation Index, NDVI: Normalized Difference Vegetation Index, LAI: Leaf Area Index, LSWI: Land Surface Water Index, EF: Evaporative Fraction, SW: Surface Soil Moisture, VPD: Vapor Pressure Deficit, Pre: Precipitation, RH: Relative Humidity, PAR: Photosynthetically Active Radiation, and T: Air Temperature. NF: Needle-leaved Forest; DBF: Deciduous Broadleaved Forest; MF: Mixed Forest; EBF: Evergreen Broadleaved Forest; SAV: Savannas; GRA: Typical Grassland; MEA: Alpine Meadow; SHR: Shrubs; SC: Single Cropping; DC: Double Cropping. In the formulas for EVI and NDVI, R_{nir}, R_{red}, R_{blue}, R_{swir} represent the surface reflectance in the near-infrared (NIR), red, and blue spectral bands, respectively. In the EF calculation formula, LE refers to latent heat flux, while H represents sensible heat flux. In the RH formula, e is the actual vapor pressure, e_s is the saturation vapor pressure, T_d is the dew point temperature, and T is the air temperature.

2.3.2 Automated Machine Learning (AutoML)

Instead of applying a specific ML method like RF for building regression models, we utilize the lightweight Python library "FLAML" version 2.3.3 (Wang et al., 2021) for the AutoML task (Metin and Bilgin, 2024). FLAML optimizes the search process by balancing computational cost and model error, iteratively selecting the learner, hyperparameters, sample size, and resampling strategy (Wang et al., 2021).

265   For our regression tasks, AutoML was configured with the "auto" option for the

266 estimator list, focusing on optimizing the R^2 metric and using a time budget of 120

267 seconds per run. Under this "auto" setting, FLAML explores a variety of built-in

268 regression estimators, including:

269   1.   LightGBM (Ke et al., 2017): a histogram-based gradient boosting method designed

270   for speed and scalability;

271   2.   XGBoost (Chen and Guestrin, 2016): a regularized gradient boosting framework

272   known for its robustness and accuracy;

273   3.   CatBoost (Prokhorenkova et al., 2018): efficiently handles categorical features and

274   reduces overfitting via ordered boosting;

275   4.   Random Forest (Breiman, 2001): an ensemble method utilizing bootstrap

276   aggregation of decision trees;

277   5.   Extra Trees (Geurts et al., 2006): enhances randomness in split point selection for

278   tree construction;

279   6.   Histogram-based Gradient Boosting (Brownlee, 2020), accelerate training through

280   feature binning;

281   7.   K-Nearest Neighbors (Cover and Hart, 1967): a non-parametric distance-based

282   algorithm relying on local data density;

283   8.   Transformer models (Vaswani et al., 2023), deep learning architectures leveraging

284   self-attention mechanisms, adapted here for structured data regression.

285   Collectively, these estimators span a broad algorithmic spectrum, including

286 ensemble learning, distance-based methods, and neural networks, enabling FLAML to

287   automatically identify the optimal model architecture for the dataset and objective.

2.3.3 Model development

289   Eighteen FLAML-LUE model variations were constructed for all sites by

290   combining different permutations of six input factor groups, as described in Eq. (3) and

291   detailed in **Table 3**. Technically, the term "FLAML-LUE" does not refer to a direct

292   implementation of a mechanistic LUE model. Instead, it reflects a hybrid modeling

293   strategy, through which we incorporate key explanatory variables that originate from

294   LUE theory—such as fPAR, light-use efficiency modifiers, and environmental stress

295   indicators (e.g., VPD, temperature, and water stress indices)—into an automated

296   machine learning framework (FLAML). These variables capture the main drivers of

297   vegetation productivity in traditional LUE models. Their integration enables FLAML

298   to build models that are both ecologically grounded and predictive, effectively

299   balancing model interpretability and accuracy.

$$GPP = f\ (PAR, T, fPAR, W_j, VT, Season) \tag{3}$$

300   where, the $fPAR$ include EVI, NDVI, and LAI; W_j denotes moisture factors including

301   LSWI, EF, SW, PDSI, Pre, RH; VT represents vegetation types, in which forest

302   ecosystems include: EBF, DBF, NF, MF, and SAV; grassland ecosystems include

303   GRA, MEA, and SHR, and farmland ecosystems include SC and DC; $Season$

304   represents the season in which the original data were acquired.

305   **Table 3**
306   Input variable combinations of fPAR and water stress indicators.

Group	Input variables	Group	Input variables	Group	Input variables
FLAML00	NDVI, LSWI	FLAML10	EVI, LSWI	FLAML20	LAI, LSWI
FLAML01	NDVI, EF	FLAML11	EVI, EF	FLAML21	LAI, EF
FLAML02	NDVI, SW	FLAML12	EVI, SW	FLAML22	LAI, SW

FLAML03	NDVI, VPD	FLAML13	EVI, VPD	FLAML23	LAI, VPD
FLAML04	NDVI, Pre	FLAML14	EVI, Pre	FLAML24	LAI, Pre
FLAML05	NDVI, RH	FLAML15	EVI, RH	FLAML25	LAI, RH

Note: EVI: Enhanced Vegetation Index, NDVI: Normalized Difference Vegetation Index, LAI: Leaf Area Index, LSWI: Land Surface Water Index, EF: Evaporative Fraction, SW: Surface Soil Moisture, VPD: Vapor Pressure Deficit, Pre: Precipitation, RH: Relative Humidity.

2.3.4 Model performance evaluation methods

To evaluate the simulation accuracy of the FLAML-LUE model in estimating GPP, we employed a suite of widely used statistical metrics to quantify the agreement between modeled and observed values (Qian et al., 2024; Chang et al., 2023; Tramontana et al., 2016). Specifically, we calculated the coefficient of determination (R^2), Pearson correlation coefficient (R), normalized unbiased root mean square error (nuRMSE), and normalized standard deviation (NSD, $\hat{\sigma}_f$), based on GPP observations from flux towers and model simulations. The Taylor diagram (Taylor, 2001) was utilized to provide a visual summary of the model's performance, incorporating R, nuRMSE, and NSD.

$$R^2 = \frac{\left[\sum_{t=1}^{T}(f_t - \bar{f})(o_t - \bar{o})\right]^2}{\sum_{t=1}^{T}(f_t - \bar{f})^2 \sum_{t=1}^{T}(o_t - \bar{o})^2} \tag{4}$$

$$R = \frac{\frac{1}{T}\sum_{t=1}^{T}(f_t - \bar{f})(o_t - \bar{o})}{\sigma_f \sigma_o} \tag{5}$$

$$nuRMSE = \frac{uRMSE}{\sigma_o} = \frac{1}{\sigma_o}\sqrt{\frac{1}{T}\sum_{t=1}^{T}\left[(f_t - \bar{f}) - (o_t - \bar{o})\right]^2} \tag{6}$$

$$\hat{\sigma}_f = \frac{\sigma_f}{\sigma_o} = \frac{1}{\sigma_o}\sqrt{\frac{1}{T}\sum_{t=1}^{T}\left((f_t - \bar{f})\right)^2} \tag{7}$$

$$\sigma_o = \sqrt{\frac{1}{T}\sum_{t=1}^{T}\left((o_t - \bar{o})\right)^2} \tag{8}$$

where, o_t represents the observed GPP from the flux tower, f_t denotes the simulated

GPP from FLAML-LUE model, $\bar{o}$ represents the average of observed GPP from the

flux tower, $\bar{f}$ represents the average of estimated GPP from the GPP product, t

represents the corresponding ID for the GPP data, and n represents the total count of

GPP data for the site. σ_o represent the standard deviations of the observed GPP. A

higher R^2 value indicates better consistency between the estimated GPP and the flux

GPP.

In addition, the Taylor Skill Score (TSS) was computed to quantitatively assess the

overall agreement between simulations and observations, with higher values indicating

better performance.

$$TSS = \frac{4(1 + R)}{\left(\hat{\sigma}_f + \frac{1}{\hat{\sigma}_f}\right)^2 (1 + R_0)} \tag{9}$$

where σ_f represent the standard deviations of the model simulation, and R_0 denotes the

maximum possible correlation coefficient (in this study, $R_0 = 1$). The TSS ranges from

0 to 1, with a higher TSS indicating better overall model performance relative to the

observations.

To further investigate model bias across sites, the percent bias (PBias) was

introduced (Qian et al., 2024). Positive PBias values indicate overestimation by the

model, while negative values suggest underestimation. The closer the PBias is to zero,

the more accurate the model's estimations. The calculation formula is as follows:

$$PBias = \frac{\sum_{t=1}^{T}(f_t - o_t)}{\sum_{t=1}^{T} o_t} \times 100\% \qquad (10)$$

338   To evaluate the model's ability to capture GPP dynamics under extreme climate

339   conditions, we identified heatwaves and high VPD events using the 95th percentile of

340   historical meteorological records (Stefanon et al., 2012; Anderson and Bell, 2010).

341   Drought events were defined as months with SPEI less than -1.5 (Ayantobo et al., 2019;

342   Gumus, 2023) . These definitions enabled us to evaluate model performance under

343   extreme environmental stresses (Qian et al., 2024, 2023).

$$CV_{Rmse} = \frac{\sqrt{\frac{1}{T}\sum_{t=1}^{T}(f_t - o_t)^2}}{\bar{o}} \times 100\% \qquad (11)$$

344   To determine whether model performance differed significantly across temporal

345   resolutions (daily, 8-day, 16-day, and monthly), we conducted paired t-tests at a 0.05

346   significance level. All statistical analyses were performed in Python 3.9 using libraries

347   including numpy, pandas, scipy, matplotlib, sklearn, and flaml. Complementary

348   visualizations were produced in R using ggplot2, ggpubr, and readxl.

349 **3. Results**

350 **3.1 Overall Model Evaluation Based on Ground-Based Observations**

351   To evaluate the model performance at the site level, the accuracy of the 18 FLAML-

352   LUE models was assessed using test datasets from individual flux tower sites. The

353   algorithms selected by each FLAML-LUE model are listed in **Table S1**. Notably, the

354   Extra-Trees algorithm was most frequently chosen as the best-performing model. Extra

355   Trees is an ensemble method that constructs multiple unpruned decision trees and

356   introduces high randomness in both feature and threshold selection, which enhances

357   generalization and reduces overfitting, particularly in noisy or high-dimensional

358   datasets. The consistent selection of Extra Trees suggests that FLAML tends to favor

359   models with higher stochasticity and ensemble structures under the given data and

360   computational constraints.

361   **Figure 3** presents the R, nuRMSE, and NSD values for the 18 models. As shown

362   in **Figure 3u**, the model performance shows relatively small differences across different

363   combinations of input indicators. Specifically (**Table 4**), the overall R^2 of the different

364   FLAML-LUE models ranged from 0.78 to 0.82, while nuRMSE values ranged from

365   0.4240 to 0.4670.

366   Among the fPAR-related indices, the model driven by EVI performed slightly

367   better ($R^2 = 0.82$, nuRMSE = 0.4265) than those driven by NDVI ($R^2 = 0.80$, nuRMSE

368   = 0.4524) and LAI ($R^2 = 0.79$, nuRMSE = 0.4561). Regarding moisture stress indicators,

369   the model using LSWI as input achieved the best performance ($R^2 = 0.82$, nuRMSE =

370   0.4298), followed by those using VPD ($R^2 = 0.80$, nuRMSE = 0.4455) and RH ($R^2 =$

371   0.80, nuRMSE = 0.4450). Models driven by EF ($R^2 = 0.80$, nuRMSE = 0.4487), SW

372   ($R^2 = 0.80$, nuRMSE = 0.4505), and Pre ($R^2 = 0.80$, nuRMSE = 0.4503) performed

373   slightly worse, though the differences were minimal.

374   As shown in **Table 5**, the performance of the FLAML-LUE model varies

375   considerably across different sites, with the average R^2 ranging from 0.17 at DXG to

376   0.92 at CBF and HBG_G01. Notably, this variation was primarily attributed to site-

377   level differences rather than the combinations of input indicators (**Figure 3**),

378   highlighting the influence of land cover type and climatic conditions on model

379   performance.

380   The best model performance was observed at the HZF, MEF, CBF and HBG_G01

381   sites ($R^2 > 0.85$, TSS > 0.9), followed by QYF, DLG, JZA, and SYA ($R^2 > 0.75$, TSS >

382   0.88). Within forest ecosystems, the model performed better in MF, NF, and DBF than

383   in EBF (ALF, BNF) and savannas (YJF). MF, which include both evergreen conifers

384   and deciduous broadleaf species, exhibit distinct seasonal variations that can be

385   effectively captured by satellite imagery. In contrast, EBF show minimal seasonal

386   greenness variation, leading to larger modeling bias in GPP estimation.

387   In grassland ecosystems, the model performed better for shrublands and typical

388   steppe than for alpine meadows (**Tables S4 and S5**). Alpine meadows, characterized

389   by short growing seasons and harsh high-altitude climates, often experience strong

390   environmental disturbances and large GPP fluctuations, making them more difficult to

391   model accurately. In contrast, typical steppe and alpine shrublands display clearer

392   phenological rhythms and stronger photosynthetic activity, making their GPP dynamics

393   easier to capture.

394   In cropland ecosystems, all sites demonstrated relatively strong model performance

395   ($R^2 > 0.6$, TSS > 0.80). Compared to natural grasslands or alpine meadows, croplands

396   are usually monocultures with stable phenology and simpler canopy structures, which

397   aid in more accurate GPP modeling.

398   Notably, at the DXG site, the model achieved a high TSS (0.8326) but a relatively

399   low R^2 (0.17), primarily due to the large performance variation among different index

400   combinations. As shown in **Table S4**, all six NDVI-driven models (FLAML10-

401 FLMAL15) have negative R² values, significantly reducing the overall model accuracy

402 at this site.

403 **Table 4**

404 Summary of evaluation metrics for FLAML-LUE model performance across all validation sites.

FLAML	R^2	R	NSD	nuRMSE	TSS
FLAML00	**0.82**	0.91	0.8806	0.4240	**0.9378**
FLAML01	0.82	0.90	0.8717	0.4301	0.9340
FLAML02	0.82	0.90	0.8810	0.4299	0.9365
FLAML03	0.82	0.91	0.8748	0.4250	0.9360
FLAML04	0.82	0.91	0.8763	0.4254	0.9363
FLAML05	0.82	0.91	0.8691	0.4244	0.9346
FLAML10	0.82	0.90	0.8638	0.4277	0.9323
FLAML11	0.79	0.89	0.8641	0.4620	0.9237
FLAML12	0.79	0.89	0.8686	0.4597	0.9256
FLAML13	0.79	0.89	0.8592	0.4539	0.9244
FLAML14	0.79	0.89	0.8629	0.4585	0.9243
FLAML15	0.80	0.89	0.8671	0.4525	0.9271
FLAML20	0.81	0.90	0.8610	0.4376	0.9291
FLAML21	0.79	0.89	0.8551	0.4542	0.9230
FLAML22	0.79	0.89	0.8597	0.4618	0.9225
FLAML23	0.79	0.89	0.8562	0.4577	0.9225
FLAML24	0.78	0.88	0.8543	**0.4670**	0.9194
FLAML25	0.79	0.89	0.8590	0.4582	0.9232
Statistics					
EVI	**0.82**	0.90	0.8756	0.4265	**0.9359**
NDVI	0.80	0.89	0.8643	0.4524	0.9262
LAI	0.79	0.89	0.8576	0.4561	0.9233
LSWI	**0.82**	0.90	0.8685	0.4298	**0.9330**
EF	0.80	0.89	0.8636	0.4487	0.9269
SW	0.80	0.89	0.8698	0.4505	0.9282
VPD	0.80	0.90	0.8634	0.4455	0.9276
Pre	0.80	0.89	0.8645	0.4503	0.9267

RH	0.80	0.90	0.8650	0.4450	0.9283

Note: The statistics represent the mean values of R², R, NSD, nuRMSE, and TSS across all combinations in which the respective variable was involved. Bold numbers indicate the highest values, while underlined numbers represent the lowest values.

Table 5

Mean evaluation metrics for different combinations of fPAR and water stress indicators at each site.

Station Name	R^2	R	NSD	nuRMSE	TSS
HZF	0.85	0.93	0.9839	0.3685	0.9650
MEF	0.91	0.96	0.8989	0.2918	0.9679
CBF	**0.92**	0.97	0.8687	0.2716	0.9644
QYF	0.75	0.89	0.8171	0.4677	0.9057
ALF	0.64	0.83	0.6250	0.5950	0.7387
DHF	0.55	0.75	0.7831	0.6671	0.8224
BNF	0.37	0.67	0.8119	0.7540	0.8003
YJF	0.43	0.68	0.6702	0.7348	0.7130
XLG	0.49	0.75	0.9877	0.6980	0.8736
NMG	0.40	0.64	0.6334	0.7685	0.6673
DLG	0.78	0.89	0.9509	0.4543	0.9425
DMG	0.59	0.78	0.6941	0.6204	0.7742
HBG_G01	**0.92**	0.96	0.9040	0.2750	**0.9715**
HBG_S01	0.53	0.82	1.1390	0.6556	0.8945
DXG	0.17	0.83	1.3421	0.7631	0.8326
JZA	0.80	0.91	0.7697	0.4373	0.8916
GCA	0.62	0.82	0.9519	0.5950	0.9014
SYA	0.81	0.92	0.7606	0.4294	0.8854
LCA	0.64	0.80	0.7830	0.5898	0.8488
YCA	0.64	0.80	0.7117	0.5991	0.8043
All	0.80	0.90	0.8658	0.4450	0.9285
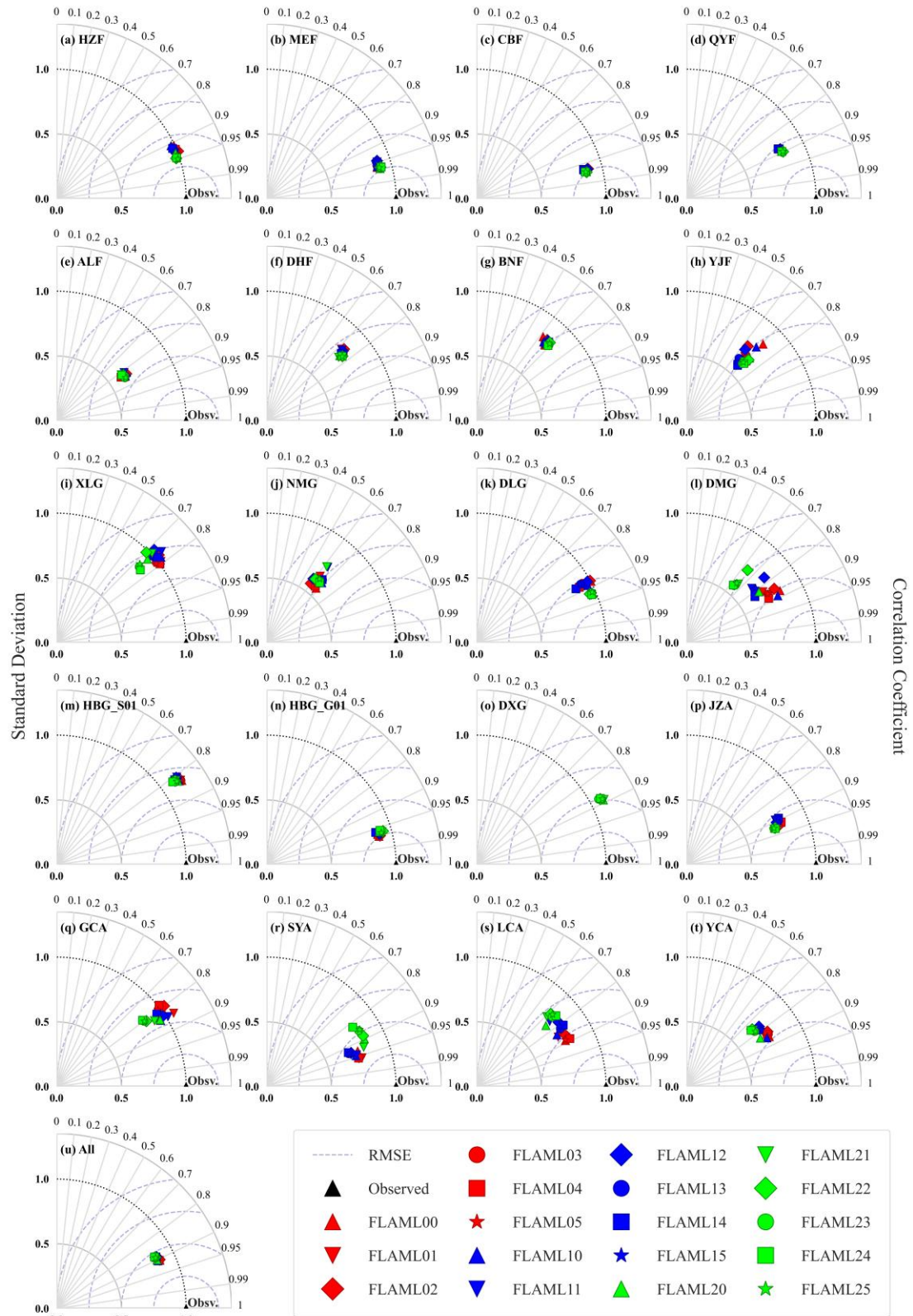
410
411 **Figure 3.** Normalized Taylor diagrams showing the performance of the FLAML-LUE model at
412 various sites based on observed GPP data. Each point represents a specific combination of fPAR
413 and water stress factor used in the model simulation. Different colors denote different fPAR products:
414 red for EVI, blue for NDVI, and green for LAI. Marker shapes indicate the type of water stress

415 factor: "+" for LSWI, "×" for EF, diamond for SW, circle for VPD, square for Pre, and star for RH.
416 Points closer to the reference point (R = 1, NSD = 1) indicate better agreement between simulated
417 and observed GPP. Panels (a)–(h) correspond to eight forest sites, (i)–(o) to seven grassland sites,
418 (p)–(t) to five cropland sites, and (u) presents an overall model evaluation on the validation dataset
419 across all sites.

420 From an ecosystem perspective, **Table 7** indicate that the FLAML-LUE model

421 achieves the highest fitting accuracy in forest ecosystems (R^2 = 0.83, nuRMSE =

422 0.4162), followed by cropland ecosystems (R^2 = 0.72, nuRMSE = 0.5258), and the

423 lowest in grassland ecosystems (R^2 = 0.71, nuRMSE = 0.5407). The slope of the fitted

424 line in **Figure 7** is less than 1 for all ecosystem types, indicating that the FLAML-LUE

425 model tends to underestimate GPP, particularly in croplands and grasslands.

426 **Tables S2, S3,** and **Table 6** collectively demonstrate that the model's performance

427 varies across ecosystem types depending on the choice of fPAR-related variables. In

428 forest ecosystems, the model is relatively insensitive to different fPAR and water-

429 related inputs, with the LAI-driven model achieving the best performance. This can be

430 attributed to LAI's ability to capture forest canopy structure, thereby improving fPAR

431 estimates. In contrast, the model's performance is more sensitive to the choice of input

432 variables in cropland and grassland ecosystems. In croplands, the EVI-driven model

433 performs best, followed by LAI and then NDVI, although the performance differences

434 are moderate. In grasslands, however, the NDVI-driven model performs worst,

435 especially at the DXG site, likely due to NDVI's sensitivity to soil background and

436 saturation in sparse and heterogeneous vegetation. EVI, with reduced saturation and

437 higher sensitivity to biomass, shows better performance in structured cropland areas.

438 Overall, the EVI and LSWI driven model (FLAML00) exhibits the best performance

439 across all ecosystem types.

440   To further investigate model accuracy across different land cover types, **Figure 5**

441   presents the R² values of five forest types, three grassland types, and two cropland types

442   under different models. In general, model performance varies little within the same land

443   cover type but differs substantially across types. Specifically, DBF, NF, MF, and SC

444   exhibit higher simulation accuracy, followed by GRA, SHR, and DC, while EBF, SAV,

445   and MEA perform the worst. These results are consistent with the Taylor diagram in

446   **Figure 3**.
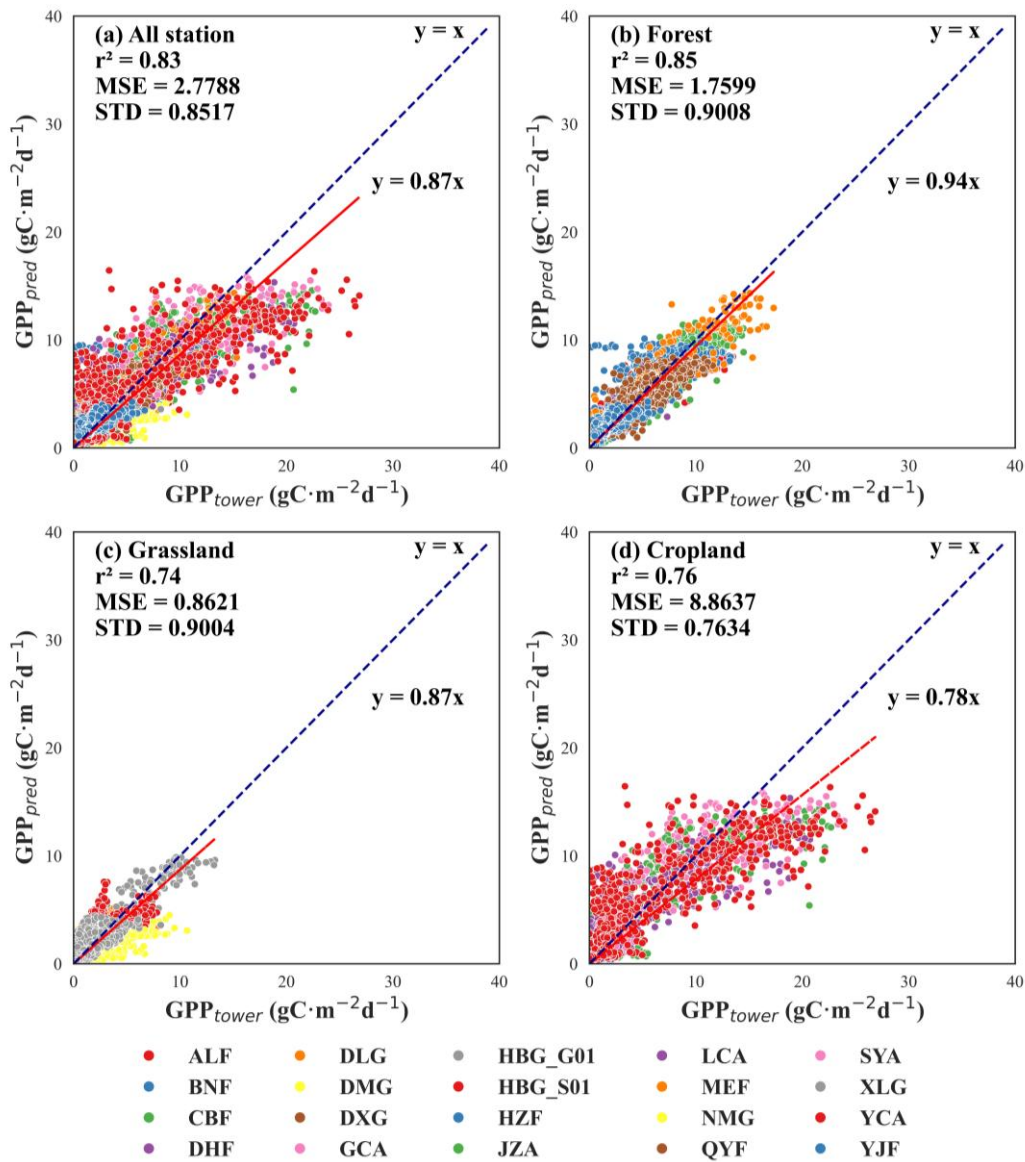
447
448 **Figure 4.** Scatterplot of observed GPP vs. simulated GPP. Different colored dots represent different
449 sites. Note: The simulated GPP values represent the mean of FLAML00 to FLAML25.

450

451 **Table 6**

452 Summary of evaluation metrics for FLAML-LUE model performance across all validation sites.

FLAML	R^2			TSS		
	Forest	Grass	Crop	Forest	Grass	Crop
FLAML00	0.83	0.73	0.77	0.9476	0.9241	0.9004
FLAML01	0.84	0.71	0.75	0.9472	0.9187	0.8946
FLAML02	0.84	0.70	0.75	0.9516	0.9167	0.8966
FLAML03	0.84	0.71	0.76	0.9485	0.9169	0.8971
FLAML04	0.84	0.72	0.76	0.9475	0.9157	0.8991
FLAML05	0.84	0.72	0.76	0.9487	0.9171	0.8927
FLAML10	0.83	0.72	0.76	0.9463	0.9213	0.8861
FLAML11	0.83	0.68	0.70	0.9464	0.9124	0.8696
FLAML12	0.84	0.67	0.70	0.9487	0.9091	0.8717
FLAML13	0.83	0.69	0.71	0.9459	0.9083	0.8696
FLAML14	0.83	0.69	0.70	0.9450	0.9060	0.8713
FLAML15	0.84	0.69	0.71	0.9486	0.9096	0.8746
FLAML20	0.85	0.73	0.73	0.9525	0.9219	0.8718
FLAML21	0.85	0.71	0.70	0.9531	0.9186	0.8575
FLAML22	0.86	0.70	0.68	0.9549	0.9150	0.8545
FLAML23	0.86	0.71	0.69	0.9539	0.9153	0.8535
FLAML24	0.85	0.72	0.67	0.9532	0.9145	0.8465
FLAML25	0.86	0.71	0.68	0.9542	0.9163	0.8561
Statistics						
EVI	0.84	**0.72**	**0.76**	0.9485	0.9182	0.8968
NDVI	0.83	0.69	0.72	0.9468	0.9111	0.8738
LAI	**0.85**	0.71	0.69	0.9536	0.9169	0.8566
LSWI	0.84	**0.73**	**0.75**	0.9488	0.9224	0.8861
EF	0.84	0.70	0.72	0.9489	0.9166	0.8739
SW	0.84	0.69	0.71	0.9517	0.9136	0.8743
VPD	0.84	0.70	0.72	0.9495	0.9135	0.8734
Pre	0.84	0.71	0.71	0.9486	0.9121	0.8723
RH	0.84	0.70	0.72	0.9505	0.9143	0.8745

453

Table 7

Mean evaluation metrics for different combinations of fPAR and water stress indicators across various ecosystems.

Ecosystem	R^2	R	$\hat{\sigma}_f$	nuRMSE	TSS
ALL	0.80	0.90	0.8658	0.4450	0.9285
Forest	**0.83**	0.91	0.8958	0.4162	**0.9431**
Grassland	0.71	0.84	0.9187	0.5407	0.9154
Croplands	0.72	0.85	0.7893	0.5258	0.8757

Note: The evaluation metrics for all sites and different ecosystem types were calculated based on the average of 18 simulation results.

Regarding CV_{RMSE}, SHR shows the largest error, followed by MEA, GRA, SC, and DC, while the five forest types show the smallest errors. This may be attributed to the greater GPP variability in grassland and cropland ecosystems, which are more strongly influenced by climatic variability and anthropogenic activities, leading to higher model uncertainty. In contrast, forest ecosystems have more stable structures and continuous carbon exchange processes, resulting in more robust model performance. Although alpine meadow is classified as grassland ecosystems, their extreme climatic conditions, short growing season, and high sensitivity to temperature and precipitation further increase the uncertainty of GPP simulation, leading to higher errors.

In terms of PBias, SHR consistently shows a pronounced overestimation across all models. Similarly, SAV and MEA are also generally overestimated in all models, though to a lesser extent than SHR. EBF exhibits a slight overestimation as well. Other vegetation types display only minor underestimation or overestimation. Overall, the models perform best for DBF, NF, and MF, followed by EBF, MEA, SC, and DC, while the simulation accuracy is relatively poor for SAV, SC, and especially SHR.

Biases also differ among grassland ecosystems, especially for typical grasslands,

475   alpine meadows, and shrublands. Typical grasslands tend to be underestimated, while

476   alpine meadows and shrublands are often overestimated. These biases may result from

477   the model's limited ability to capture seasonal changes in water availability and its

478   interaction with temperature. Typical grasslands usually show high productivity when

479   water is sufficient, especially in spring and summer. If the model fails to reflect these

480   seasonal patterns, it can lead to underestimation. In contrast, productivity in alpine

481   meadows is mainly limited by low temperatures and a short growing season. If the

482   model does not fully consider these constraints, it may overestimate photosynthesis and

483   thus GPP. For shrublands, overestimation may be due to high spatial heterogeneity,

484   including a mix of shrubs, grasses, and bare soil. This complexity is difficult to capture

485   in remote sensing data (e.g., fPAR) and model inputs, leading to possible overestimation

486   of productivity.
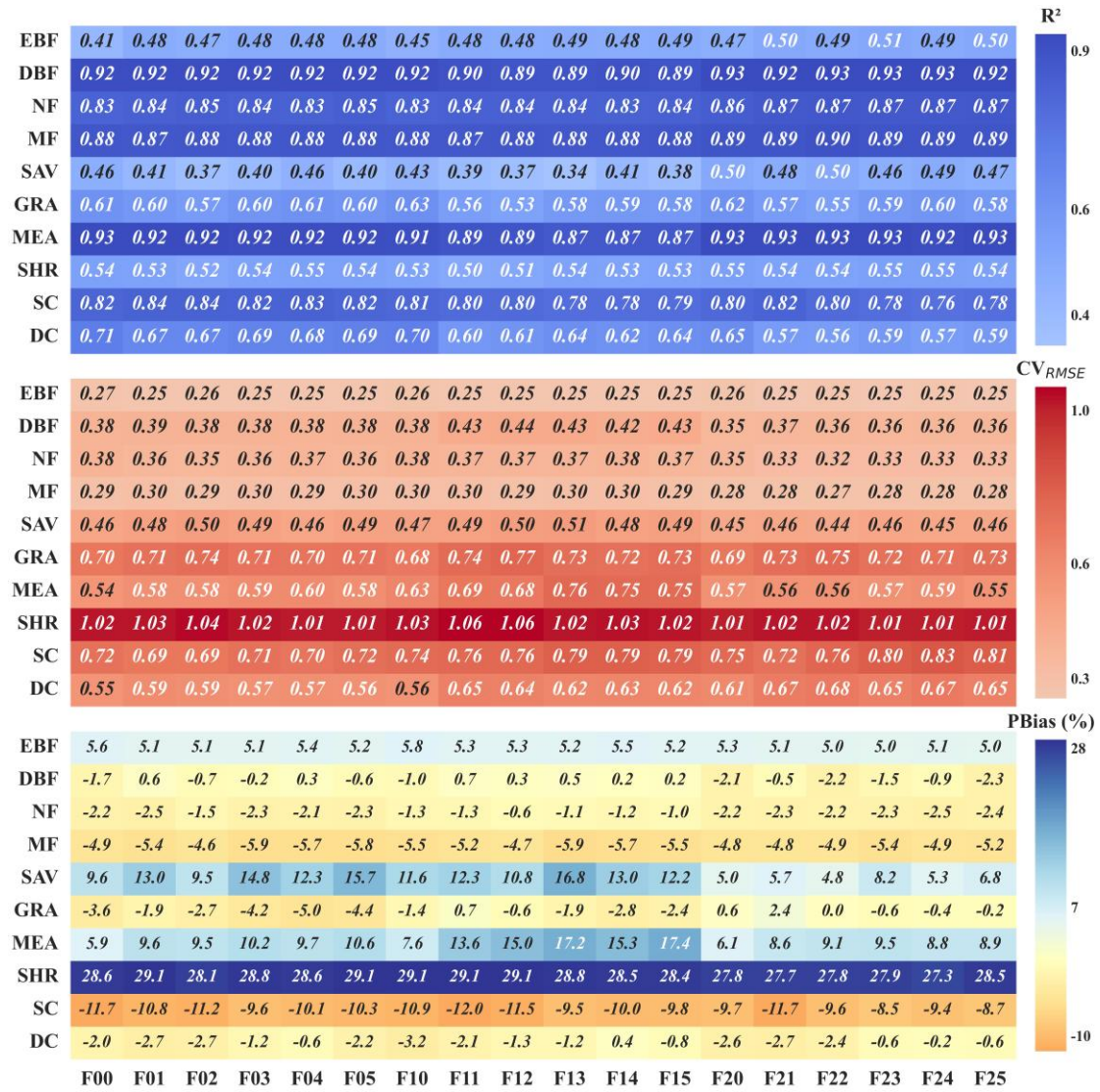
Figure 5. Comparison of R², CV$_{RMSE}$, and PBias of GPP estimates from different FLAML-LUE models across various land cover types. Note: F00 represents FLAML00, and so on.

Across the four temporal scales, the performance of the 18 FLAML-LUE models improves as the temporal resolution becomes coarser. The average R² across 20 sites increases from 0.64 at the daily scale to 0.74 at the monthly scale (**Table S8**), while the average nuRMSE decreases from 0.5518 to 0.4088. Paired t-tests show that, except for YJF, NMG, DMG, DXG, and YCA, the FLAML-LUE model exhibits significantly lower R² at the daily scale than at longer temporal scales ($p < 0.05$, **Figure 6**). For these five sites, model performance remains relatively stable across different temporal scales.

Furthermore, compared to the daily scale, the nuRMSE decreases by 12.97%,

16.52%, and 25.92% at the 8-day, 16-day, and monthly scales, respectively, indicating

that the uncertainty of the FLAML-LUE model is significantly reduced at coarser

temporal resolutions.
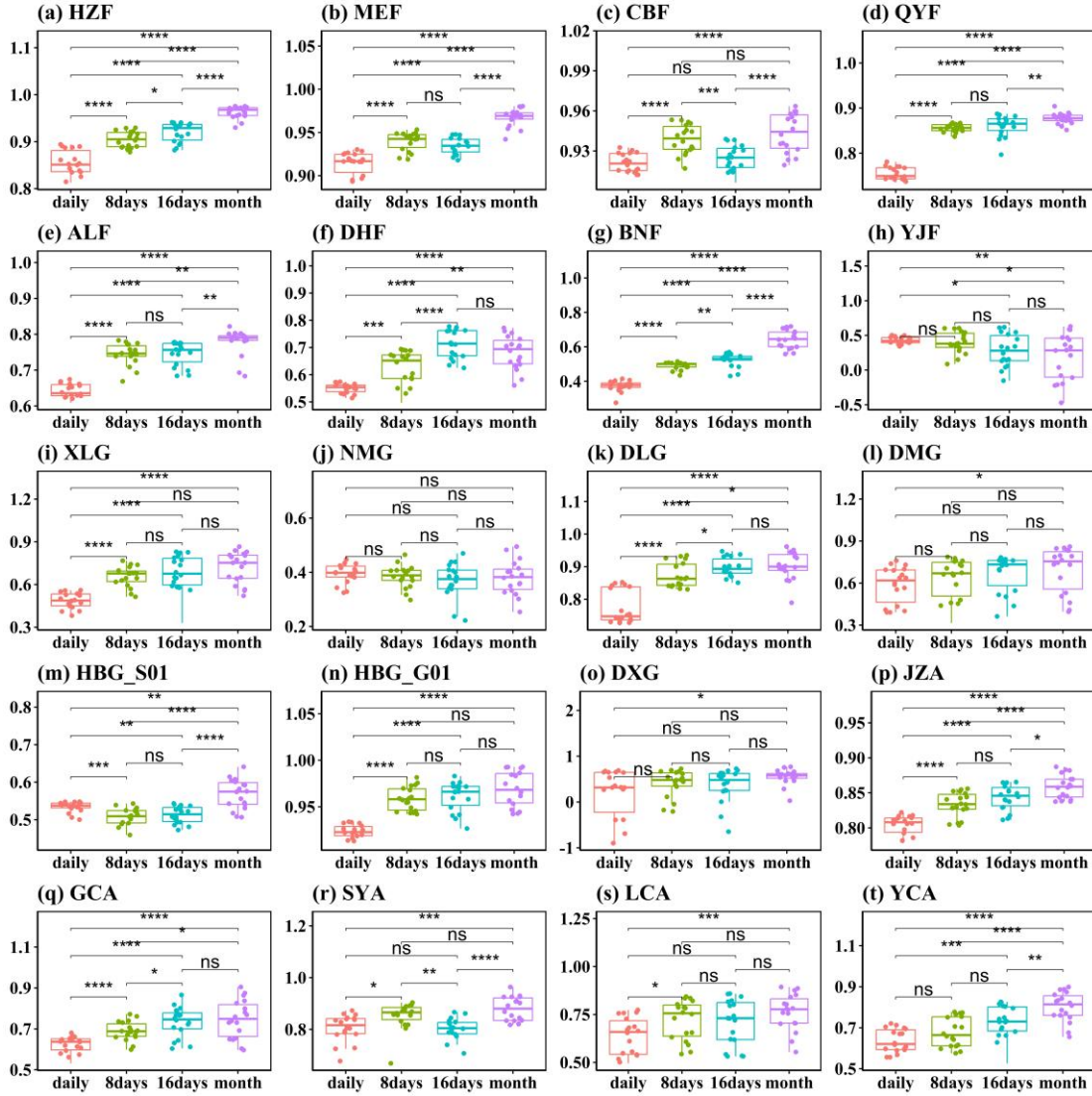
Figure 6. Asterisks indicate significant differences between the R^2 at the four temporal resolutions (Kruskal-Wallis test), ****p values < 0.0001, ***p values < 0.001, **p values < 0.01, *p values ⩽ 0.05, and ns indicates no significance (p > 0.05).

Overall, the accuracy of FLAML-LUE models constructed using different

combinations of fPAR and water stress indicators showed limited variation, with the

FLAML00 model (fPAR = EVI, water = LSWI) demonstrating the best performance.

However, the model exhibited considerable differences in performance across

ecosystem types, with the highest accuracy observed in forest ecosystems, followed by

croplands and then grasslands. Further analysis by specific vegetation cover types

revealed that the model performed best for DBF, NF, and MF, followed by GRA, MEA

SC, and DC, while its performance was relatively poor for EBF, SAV, and particularly

SHR (PBias > 27%, CVrmse > 1, R^2 < 0.6). In addition, evaluation across different

temporal scales indicated that model uncertainty decreased with increasing time

intervals, suggesting that the FLAML-LUE model exhibits greater robustness and

reliability at coarser temporal resolutions.

3.2 Model Evaluation Under Extreme Climatic Conditions

Numerous studies have demonstrated that climate extremes such as heatwaves,

droughts, and high atmospheric VPD can substantially alter ecosystem dynamics and

reduce carbon uptake capacity (Frank et al., 2015; Reichstein et al., 2013). These

extreme events can suppress photosynthesis, increase respiration, and disrupt the

balance of carbon exchange between vegetation and the atmosphere. In order to

evaluate the robustness and reliability of the FLAML-LUE models under such stress

conditions, this study further investigates model performance in simulating GPP under

three types of climate extremes: high temperature, high VPD, and drought. By

analyzing the response of model accuracy and bias under these scenarios, we aim to

assess its applicability and limitations in extreme environmental conditions.

3.2.1 Performance Under High Temperature Events

Figure 7 shows the performance of 18 FLAML-LUE models under high-

temperature and non-high-temperature conditions. The results indicate a significant

decline in model accuracy under high-temperature conditions. As shown in **Figure 7a**, the models perform well under non-high-temperature conditions, with the R values of all 18 FLAML-LUE models exceeding 0.9. However, under high-temperature conditions, the Taylor diagram reveals a significant decrease in model performance, with correlation coefficients dropping and a substantial increase in nuRMSE, indicating a reduced ability to capture GPP dynamics.

Interestingly, as shown in **Figure 7b**, the CV_{RMSE} values under non-high-temperature conditions are generally higher than under high-temperature conditions. This may be due to higher observed GPP values under high temperatures, resulting in a larger denominator for CV_{RMSE}, which can reduce the CV_{RMSE} despite larger prediction errors. Overall, the difference in prediction bias between high-temperature and non-high-temperature conditions is minimal.

Figure 7c shows that, under high-temperature conditions, the PBias fluctuates more significantly, with more stations showing severe overestimation or underestimation. Specifically, some models (e.g., FLAML00, FLAML01, FLAML11, FLAML15, FLAML21) overestimate GPP at certain sites under high-temperature conditions, while all models show more severe underestimation at other sites. Models driven by LAI (FLAML20 – FLAML25) exhibit smaller bias variations under non-high-temperature conditions, with PBias mainly ranging from -0.3 to 0.3.

In conclusion, high-temperature conditions increase model uncertainty, with all models exhibiting varying degrees of overestimation or underestimation across sites. Models incorporating VPD, precipitation, and relative humidity as water stress factors

553 perform better overall, indicating greater robustness under high-temperature stress.
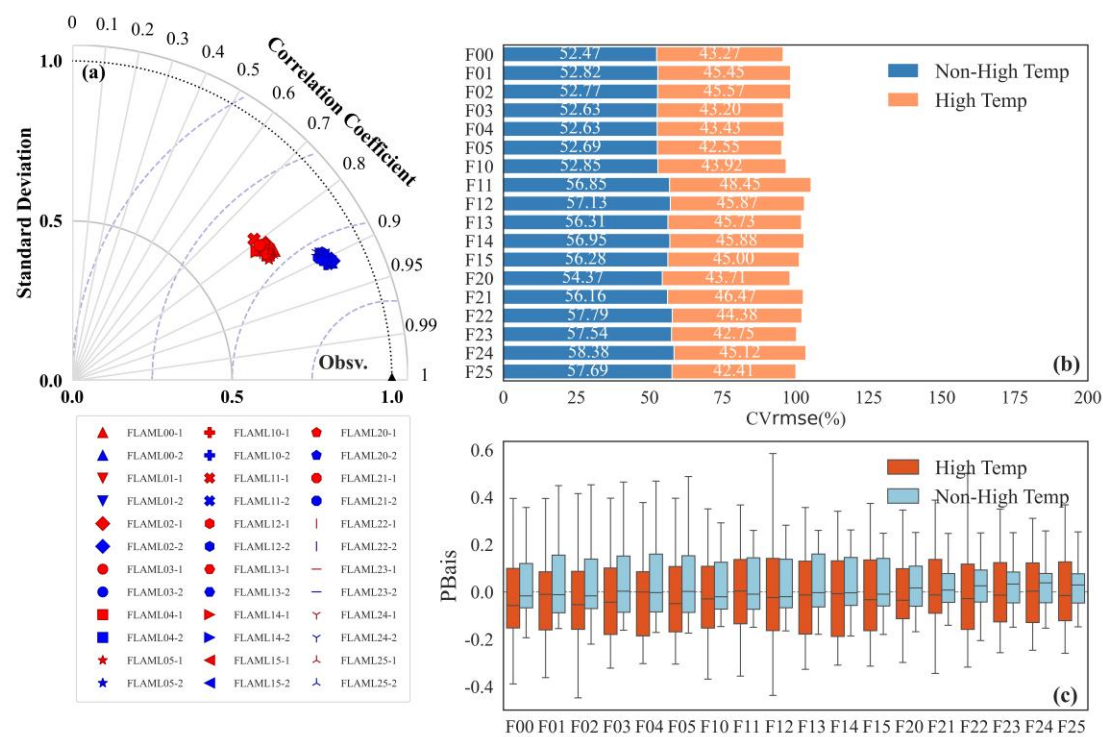
555 **Figure 7**. The comparison of GPP products performance under high temperature and non-high
556 temperature (In the Taylor diagram, 1 represents high temperature, 2 represents non-high
557 temperature).

558 Differences in model performance under high-temperature and non-high-

559 temperature conditions are pronounced across various land cover types. **Figure 8**

560 compares the estimation accuracy of different land cover types under both conditions.

561 Overall, model accuracy in simulating GPP is significantly lower under high-

562 temperature conditions, with R^2 values showing a notable decline. Specifically, for the

563 NF type, the R^2 under high temperatures approaches a negative value, indicating very

564 low explanatory power, whereas under non-high-temperature conditions, R^2 ranges

565 from 0.83 to 0.87. Notably, the FLAML13 model for Savannas shows a drastic decrease

566 in R^2 from 0.38 under non-high-temperature conditions to -1.46 under high-temperature

567 conditions, performing even worse than the mean of the data during high temperatures.

568   Corresponding to **Figure 7**, CV_{RMSE} is generally lower under high-temperature

569 conditions than under non-high-temperature conditions. The SHR type exhibits a higher

570 coefficient of variation, while PBias shows more pronounced fluctuations. For SHR

571 and EBF, the models tend to overestimate GPP under both temperature conditions, with

572 overestimation more pronounced under high temperatures. In contrast, MEA shows

573 underestimation under high-temperature conditions but overestimation under non-high-

574 temperature conditions. Overall, most land cover types exhibit a greater degree of

575 underestimation under high-temperature conditions. Nevertheless, the MF type

576 maintains relatively high simulation accuracy. In contrast, the NBF, NF, and SC types

577 are more strongly affected by high temperatures, with NF showing negative simulation

578 accuracy under high-temperature conditions and SC exhibiting marked variations in

579 PBias.
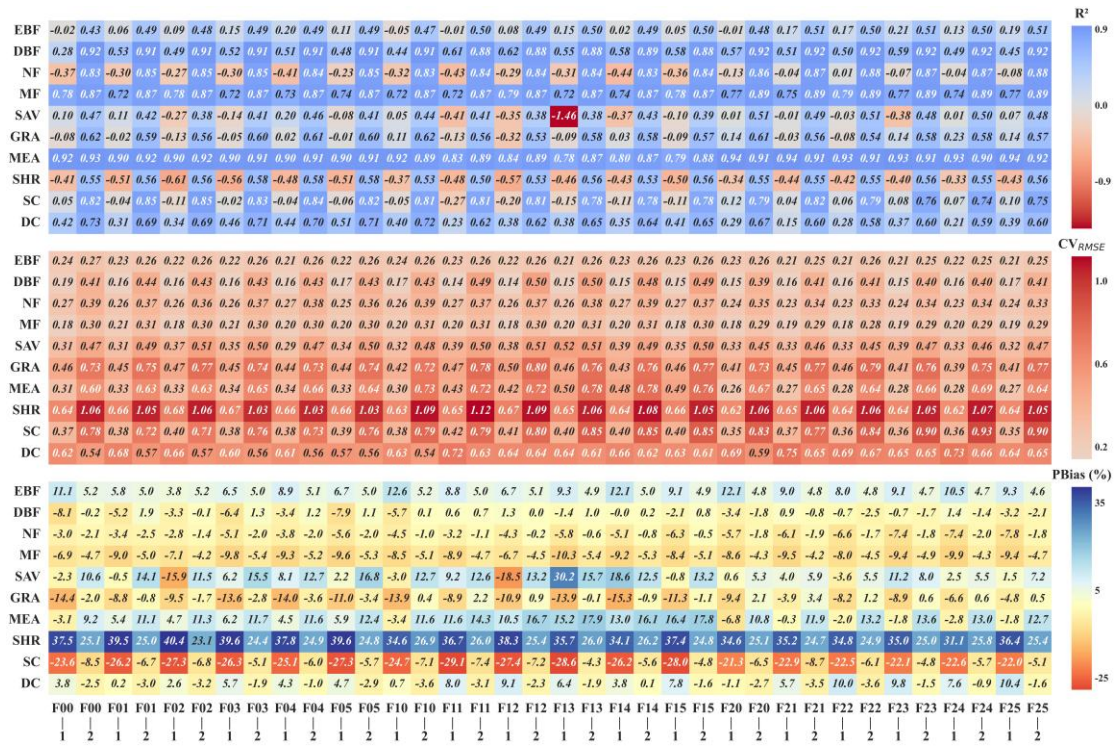
Figure 8. Comparison of statistical indicators (R^2, CV_{RMSE}, PBias) of FLAML-LUE model under high temperature conditions and non-high temperature conditions for different land cover types (1 represents high temperature, 2 represents non-high temperature).

3.2.2 Performance Under High VPD

Figure 9 shows the performance of the 18 FLAML-LUE models under high and non-high VPD conditions. Unlike the high-temperature scenario, the statistical metrics of all models exhibit only a slight decline under high VPD, indicating a less pronounced impact on model performance. As shown in **Figure 9a**, the variability in model performance increases under high VPD conditions. However, **Figure 9b** reveals that CVRMSE values are generally higher under non-high VPD conditions, a trend consistent with the results observed under high-temperature conditions.

Under high VPD, PBias exhibits significant fluctuations compared to non-high VPD conditions (**Figure 9c**). Specifically, the average PBias across sites is higher under high VPD, whereas it is lower under non-high VPD. In high VPD conditions, models

driven by EVI show smaller differences in PBias across sites, with values primarily ranging from -0.4 to 0.5. In contrast, FLAML05 shows larger differences in PBias between sites under non-high VPD, with overestimations at some sites. Overall, model performance under high VPD shows greater uncertainty, with both overestimations and underestimations occurring across different sites. In general, EVI-driven models perform more consistently under both high and non-high VPD conditions.

Model performance also differs across land cover types under high and non-high VPD conditions. **Figure 10** compares the estimation accuracy for various land cover types under both conditions. Overall, GPP simulation accuracy for certain cover types (e.g., DBF, MF, MEA, SC, DC) shows little difference between high and non-high VPD conditions. Although R^2 values for some land cover types are significantly lower under high VPD than under non-high VPD, the impact of high VPD on model performance is smaller compared to high temperature. The most notable example is the FLAML13 model for Savannas, where R^2 drops significantly from -1.46 under non-high VPD to -0.39 under high VPD, performing worse than the mean data value under high VPD.

Similar to high-temperature conditions, CV_{RMSE} under high VPD is generally lower than under non-high VPD. MEA shows a larger coefficient of variation, and PBias exhibits more noticeable fluctuations. For the EBF and SHR type, models tend to overestimate GPP in both high and non-high VPD conditions, with the overestimation being more pronounced under high VPD. SC and GRA models show significant underestimation under high VPD. DBF, NF, and MF perform relatively well under high VPD, while SC underestimates GPP under both conditions, and DC overestimates GPP

under high VPD but underestimates it under non-high VPD. Overall, compared to high-

temperature conditions, the effect of high VPD on estimation errors is smaller across

different land cover types.
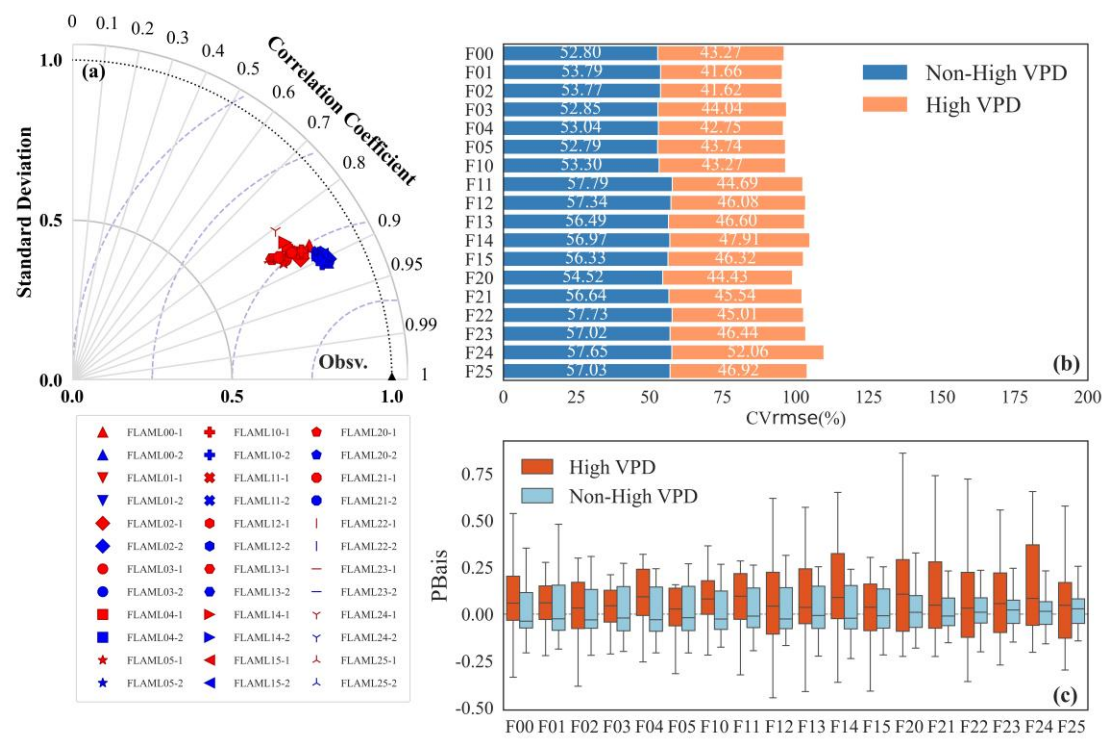
Figure 9. The comparison of GPP products performance under high VPD and non-high VPD (In the Taylor diagram, 1 represents high VPD, 2 represents non-high VPD).
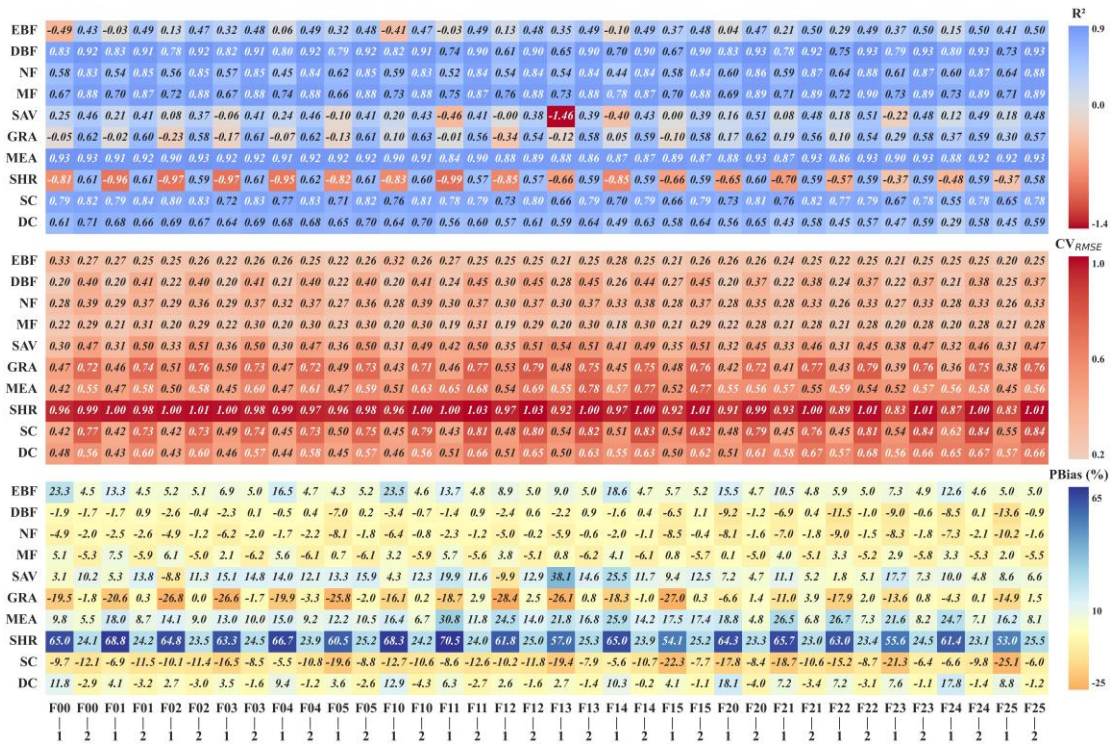
Figure 10. Comparison of statistical indicators (R^2, CV_{RMSE}, PBias) of FLAML-LUE model under high VPD conditions and non-high VPD conditions for different land cover types (1 represents high VPD, 2 represents non-high VPD).

3.2.3 Performance Under Drought Conditions

Figure 11 presents the simulation performance of the 18 FLAML-LUE models under drought and non-drought conditions. Unlike the decline in performance under high temperature and high VPD conditions, the model shows similar or even slightly better accuracy under drought compared to non-drought conditions. This may be attributed to an overall reduction in GPP and its variability during drought periods, which potentially makes it easier for the models to capture the general trend and thereby improves simulation accuracy.

Compared to the boxplots under non-drought conditions, drought notably increases the variability in PBias across sites for all models, particularly due to substantial overestimation at certain sites. In contrast, the degree of underestimation remains

similar to that under non-drought conditions. Among the models, those driven by EVI

exhibit the best overall performance, followed by those using LAI as the vegetation

indicator.

Figure 12 shows that drought substantially affects GPP estimation accuracy across

most land cover types. For certain types, such as savannas and deciduous broadleaf

forests, no data were available during drought months, making performance evaluation

under drought impossible. For other land cover types, the impact of drought varies

significantly. Specifically, EBF, MEA, and DC show higher R^2 values under drought,

while NF, MF, GRA, SHR, and SC perform better under non-drought conditions.

Among them, MF and SHR have the lowest simulation accuracy under drought but

perform relatively well during non-drought periods.

Regarding CV_{RMSE}, all land cover types except MEA and NF exhibit lower values

under drought conditions, consistent with the results in **Figure 11a**. MEA shows the

largest coefficient of variation, indicating greater variability in model performance

under drought. In terms of PBias, NF, MEA, and SHR exhibit the highest errors. On

average, model errors increase under drought across most land cover types. Except for

EBF and GRA, most types show severe overestimation or underestimation during

drought periods.

657
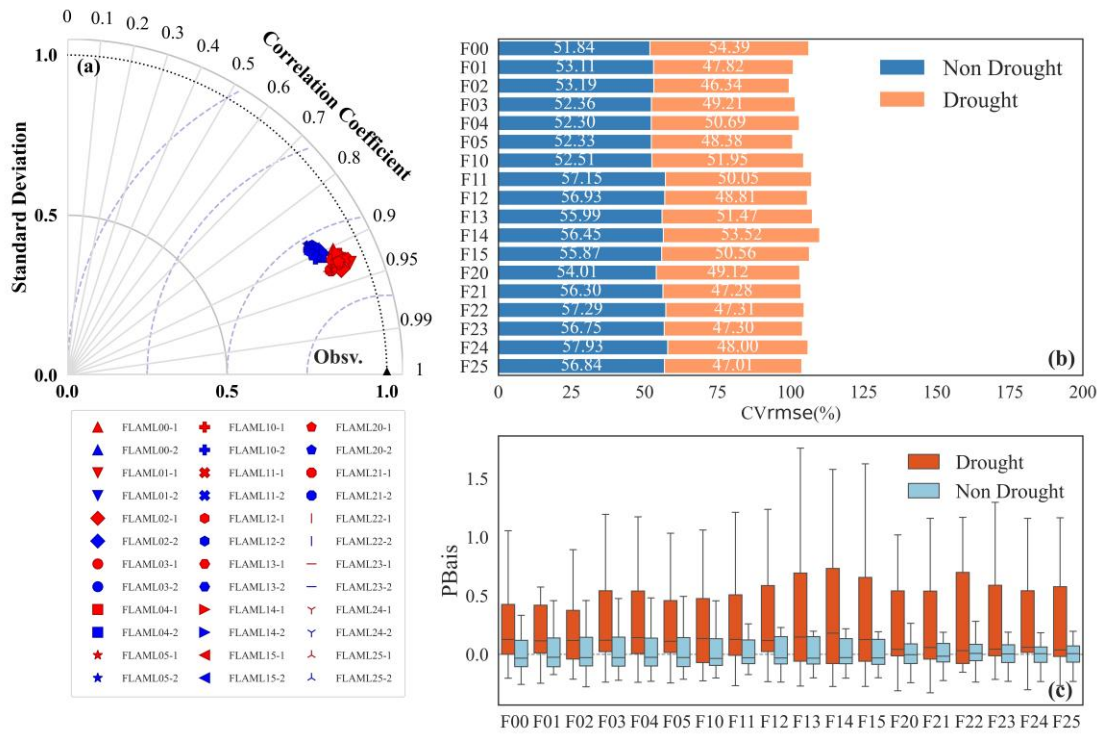
Figure 11. The comparison of GPP products performance under drought and non-drought (In the Taylor diagram, 1 represents drought, 2 represents non drought).

660
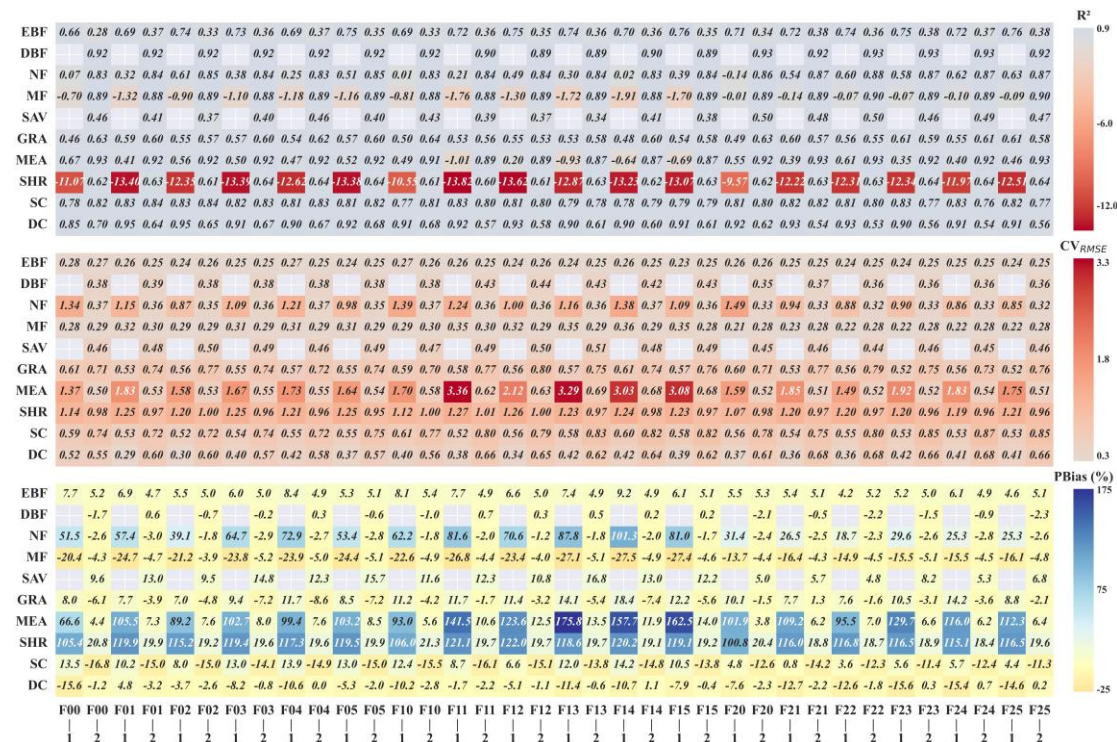
Figure 12. Comparison of statistical indicators (R^2, CV_{RMSE}, PBias) of FLAML-LUE model under drought conditions and non-drought conditions for different land cover types (1 represents drought, 2 represents non-drought).

4. Discussion

Model performance is highly influenced by the algorithms used, the underlying processes, and how GPP responds to varying environmental conditions (Chang et al., 2023). A detailed comparison of the FLAML-LUE models across different ecosystems showed that performance varied depending on the input variables, vegetation types, and time scales (Chang et al., 2023; Harris et al., 2021).

4.1 Performance comparison of FLAML-LUE models for different ecosystems

In this study, FLAML-LUE models were constructed for different combinations of variables and different time scales based on AutoML algorithms. On the whole, the modeled GPP values agree well with the GPP estimated based on the EC tower, and the FLAML-LUE models performed better in capturing the magnitude and seasonal dynamics of the GPP, which indicated that it was feasible to estimate the GPP using AutoML algorithms. Further, all three ecosystems showed good model performance driven by observational data. Comparisons across various ecosystems indicate that the model exhibited superior performance over forest ecosystems compared to grassland and agricultural ecosystems, as evidenced by the average R^2 values.

Although model performance differences across indicator combinations were minimal, EVI-driven FLAML-LUE models slightly outperformed those driven by NDVI. This highlights the key role of EVI in GPP estimation, as it offers more comprehensive atmospheric correction and is less susceptible to saturation from green reflectance compared to NDVI. Additionally, model performance varied significantly

686 across sites.

687 Based on the evaluation metrics, the optimal model selected was FLAML00 (EVI

688 + LSWI). Under this combination of indicators, the FLAML-LUE model demonstrated

689 the best performance in mixed forests at CBF, deciduous broadleaf forests at MEF, and

690 alpine meadows at HBG_G01, with R^2 values of 0.92, 0.92, and 0.93, respectively. The

691 next best performances were observed in coniferous forests at QYF and HZF, single-

692 cropping farmland at JZA and SYA stations, double-cropping farmland at YCA, and

693 typical grasslands at DLG and DMG sites. In contrast, the model performed poorly in

694 alpine shrub and alpine ecosystems, with an R^2 of 0.54, and the worst performance was

695 observed at the BNF site, with an average R^2 of only 0.28. Mixed forests exhibit distinct

696 seasonal variations that satellite imagery can effectively capture, while evergreen

697 broadleaf forests (ALF and BNF) show minimal seasonal changes in vegetation cover

698 or greenness, making accurate predictions challenging. Alpine shrublands have more

699 complex vegetation structures and less distinct seasonal variations in vegetation cover,

700 which makes it harder for the model to capture the dynamics accurately. In contrast,

701 alpine meadows exhibit more pronounced seasonal variations in vegetation cover,

702 which makes the model more effective in capturing GPP dynamics. For non-forest

703 ecosystems, the highest R^2 values were observed in agricultural fields and typical

704 grasslands, followed by alpine meadows and alpine shrublands.

705 Mixed forests display clear seasonal variations that satellite imagery can effectively

706 capture. However, evergreen broadleaf forests (ALF) have slight seasonal variations in

707 vegetation cover or greenness, making it difficult for the model to predict. For non-

708 forest ecosystems, the highest R^2 was found in agricultural fields and typical grasslands,

709 followed by alpine meadows and alpine scrub. In addition, the differences in model

710 performance were also reflected in different temporal scales. In general, the model

711 simulation performance at the 16-day and monthly scales was better than that at the

712 daily scale, and the performances of different temporal scales for forest, grassland, and

713 cropland ecosystems were consistent with previous studies.

714   This study did not distinguish between rainfed and irrigated agricultural systems,

715 considering only the crop rotation types. Specifically, JZA and SYA represent rainfed

716 systems, whereas GCA, LCA, and YCA are irrigated. Future research could incorporate

717 this distinction to improve the accuracy of carbon flux estimates in cropland ecosystems.

718 This distinction is important for interpreting model results under water-limited

719 conditions.

720   In addition, our results indicate that forest and agricultural fields have greater

721 carbon sequestration capacity and higher annual fluxes than grasslands (Table S9, S10,

722 S11), aligning with previous research outcomes (Y. Wang et al., 2021; Zhang et al.,

723 2007). However, due to the annual harvest of crops, approximately 76% of the on-farm

724 biomass is removed, resulting in limited long-term carbon storage capacity (Zhang et

725 al., 2007). With the exception of tropical rainforests (i.e., BNF), the annual carbon

726 production of planted forests (i.e., QYF) is higher than that of natural forests (i.e., CBF,

727 DHF), which implies that planted forests possess significant potential for carbon

728 assimilation, functioning as robust carbon sinks.

729

4.2 Model Performance Variations Under Extreme Conditions

In the context of global warming and the increasing frequency of extreme climate events, the adaptability and stability of GPP estimation models in extreme environments have become crucial. This study systematically evaluated the performance of the FLAML-LUE model under high-temperature, high-VPD, and drought scenarios by grouping the validation set. The results showed a general decline in the model's accuracy across all three extreme climate conditions, with varying performance depending on the scenario, highlighting the complexity of vegetation carbon absorption responses to climate stress.

In high-temperature conditions, the model generally underestimated GPP. This could be due to the suppression of photosynthesis caused by high temperatures. High temperatures increase transpiration stress, causing stomatal closure to reduce water loss, which limits CO_2 input and lowers photosynthetic rates (Qu et al., 2020; Reichstein et al., 2013). Additionally, high temperatures can cause leaf damage and senescence, reducing LAI and overall photosynthetic potential (A. Chen et al., 2021; Y. Chen et al., 2021). Although the FLAML-LUE model accounts for fPAR and water stress factors, it may not fully capture rapid responses such as leaf damage or sudden declines in LAI, which likely contribute to the reduced accuracy under high-temperature conditions. Moreover, the model does not explicitly account for the lag effect of leaf senescence, which may further worsen estimation bias (Frank et al., 2015).

Under high VPD conditions, the model showed significant uncertainty, with some areas overestimating GPP and others underestimating it. This inconsistency likely arises

752 from the diverse water stress mechanisms induced by high VPD. Guo et al. (2015) noted

753 that high VPD does not always reflect the true level of water stress in plants, leading to

754 the potential overestimation of GPP. Conversely, in extreme VPD scenarios, where

755 stomata close to reduce carbon absorption, the model may underestimate GPP if it fails

756 to recognize this regulatory behavior (Li et al., 2016). Additionally, the FLAML-LUE

757 model does not explicitly consider leaf energy load or light inhibition, which may

758 contribute to the model's higher errors under high VPD conditions (Rigden et al., 2020).

759   Although the model's performance decreased at some sites under drought

760 conditions, its overall accuracy improved under these scenarios. This improvement may

761 be due to the stronger limiting effect of drought on vegetation growth, allowing the

762 model to more accurately capture the suppressive impact of water stress on

763 photosynthesis. In drought conditions, water scarcity limits carbon absorption, leading

764 to a substantial reduction in GPP (McDowell et al., 2008). As a result, the model's

765 estimates are more likely to align with the actual limitation of carbon absorption. Thus,

766 under drought conditions, the model may underestimate GPP, which can be more

767 accurate, while in wetter environments, where water stress is less pronounced, the

768 model may overestimate GPP, reducing its accuracy. Additionally, under drought, the

769 model is likely better at capturing the direct effects of water shortage on plant

770 physiology, reducing interference from other environmental variables and improving

771 prediction accuracy (Zhou et al., 2019).

772   Although the FLAML-LUE model demonstrates strong predictive capabilities

773 under normal climate conditions, there is still room for improvement under extreme

774 scenarios. One potential limitation is the insufficient representation of rapid plant

775 response mechanisms (e.g., leaf damage and sudden declines in LAI) in the current

776 input features (Frank et al., 2015; Reichstein et al., 2013). Future research could

777 incorporate high-temporal-resolution vegetation indices, such as solar-induced

778 chlorophyll fluorescence (SIF), to better capture dynamic changes in plant metabolic

779 activity and stress responses under extreme conditions (Yi et al., 2024; Pagán et al.,

780 2019). Including lag variables or cumulative stress indices could also enhance the

781 model's ability to handle delayed physiological responses after stress events (Frank et

782 al., 2015). Furthermore, future studies should expand the scope to include a broader

783 range of climate events that affect GPP, such as floods and low temperatures, in addition

784 to high temperature, high VPD, and drought (Wang et al., 2023). Vegetation in different

785 regions responds differently to these events, with low temperatures and frost being

786 especially important for high-latitude ecosystems.

4.3 Advantages of FLAML-LUE framework

788 In this study, FLAML (Wang et al., 2021) selected the Extra Trees algorithm as the

789 best-performing model for GPP simulation in China. Extra Trees is an ensemble

790 learning method that builds multiple unpruned decision trees and incorporates

791 randomization in features selection and split thresholds determination. Compared to

792 traditional decision tree ensembles such as Random Forests, Extra Trees typically

793 achieves minimal variance while maintaining low bias, which makes it particularly

794 well-suited for complex, high-dimensional datasets (Geurts et al., 2006).

795 The adoption of FLAML provides several significant advantages. First, it

automates the model selection and hyperparameter tuning process, eliminating the need for extensive manual trial-and-error and reducing reliance on domain expertise (Nakano and Liu, 2025; Wang et al., 2022). Instead of manually evaluating various algorithms and their configurations, FLAML efficiently explores a broad search space and identifies the most appropriate model for the dataset.

Moreover, FLAML employ a cost-aware hyperparameter optimization strategy, enabling it to find high-performing models with relatively low computational cost (Zhang et al., 2023; Wang et al., 2021). This feature is particularly advantageous in scenarios with limited computational resources or the need for rapid prototyping.

Compared to conventional machine learning workflows, FLAML significantly reduces human bias in model selection, improves reproducibility, and lowers the barrier to applying advanced modeling techniques (He et al., 2021). Overall, the use of FLAML in this study not only improved model performance but also streamlined the modeling process, supporting its broader applicability in ecological and climate-related research.

4.4 Comparison with other products
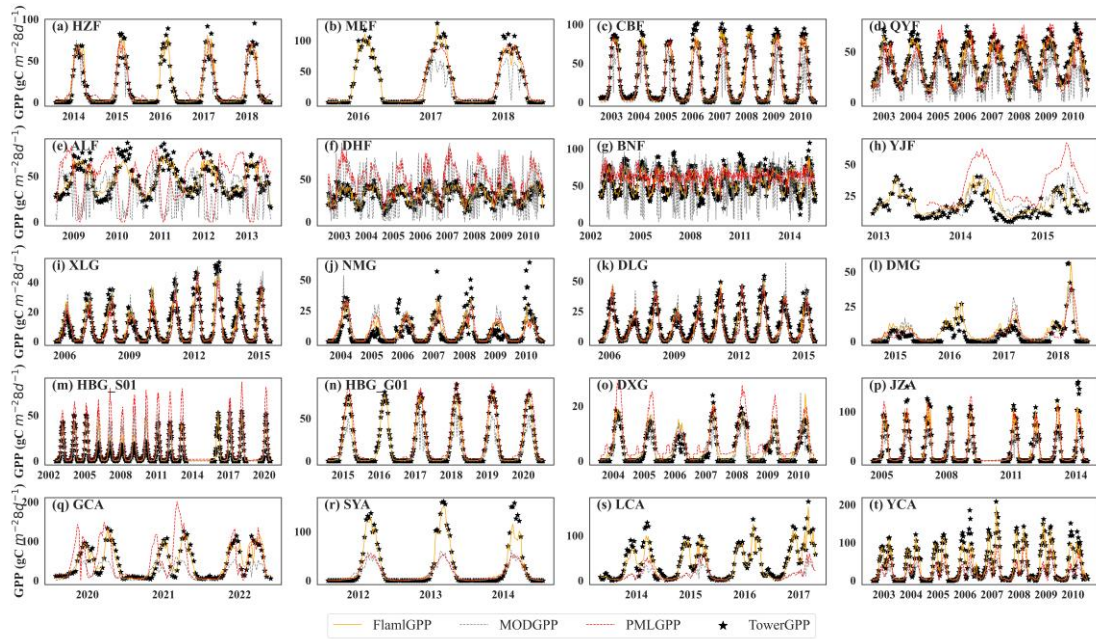
Figure 13. Comparing 8-day GPP from FLAML-LUE, PML, MOD17 models, and EC observations.

This study attempted to predict the GPP of different sites using the FLAML model based on the LUE model variables. The results showed that the AutoML algorithm is a promising GPP estimation method, which explains on average 75% - 98% of the GPP variation.

Compared to two GPP products (MODIS GPP, and PML GPP), the GPP from this study showed the highest precision (**Table 7**) and better consistency with flux tower-based GPP under different ecosystems. Overall, the FLAML-LUE model used in this study had the best simulation performance. These findings highlight the potential of the FLAML algorithm for accurately estimating GPP. The FLAML-LUE model is a data-driven ML approach that builds relationships based on dependent and explanatory variables. This enables it to effectively simulate the complex nonlinear interactions across diverse ecosystems (Tramontana et al., 2016). This advantage is even more prominent at the global scale, considering that more flux tower data are available for

826   model construction.

827   **Table 7**

828   R^2 of 8-day GPP simulated by FLAML-LUE, PML, and MOD17 at different ecosystems validation

829   sites.

Ecosystem	Station	R2			TSS		
		FLAML	MOD	PML	FLAML	MOD	PML
ALL	ALL	0.93	0.71	0.78	0.9657	0.2677	0.5675
Forest	HZF	0.95	**0.88**	0.91	0.9843	**0.9672**	0.9569
	MEF	**0.98**	0.78	**0.95**	0.9868	0.7664	**0.9571**
	CBF	0.98	0.78	0.93	**0.9903**	0.8860	0.9567
	QYF	0.95	0.54	0.74	0.9833	0.8634	0.9231
	ALF	0.87	0.24	0.34	0.9054	0.2455	0.1812
	DHF	0.83	0.27	0.45	0.9527	0.3030	0.5851
	BNF	0.81	0.05	0.02	0.9025	0.3370	0.3337
	YJF	0.75	0.31	0.42	0.9334	0.7759	0.5820
Grass	XLG	0.92	0.76	0.79	0.9651	0.9343	0.9008
	NMG	0.67	0.48	0.41	0.8288	0.8340	0.7436
	DLG	0.92	0.76	0.77	0.9787	**0.9349**	0.9320
	DMG	0.82	0.68	0.57	0.9537	0.9080	0.8611
	HBG_S01	0.89	0.78	0.81	0.9718	0.9284	0.7175
	HBG_G01	0.99	0.91	0.97	**0.9947**	0.7546	**0.9911**
	DXG	0.90	0.75	0.82	0.9737	0.9134	0.9105
Crop	JZA	0.95	0.84	0.85	**0.9786**	**0.6009**	**0.9582**
	GCA	0.89	0.33	0.19	0.9708	0.4889	0.6748
	SYA	**0.96**	**0.92**	**0.92**	0.9666	0.3708	0.3948
	LCA	0.94	0.57	0.48	0.9731	0.2433	0.3959
	YCA	0.93	0.71	0.78	0.9657	0.2677	0.5675

830   Note: Bold numbers indicate the highest values, while underlined numbers represent the lowest

831   values.

832   However, further work is needed to evaluate the FLAML-LUE model's suitability

833   and accuracy, considering its limitations. In particular, it tends to underestimate high

834   GPP and overestimate low GPP. In addition, the model performance in GPP estimation

835   is highly dependent on ecosystem type. Our findings indicated that mixed forests,

836   deciduous broadleaf forests, and agricultural lands had higher prediction accuracies.

While grass sites such as alpine scrub and alpine meadows were predicted with large uncertainties, consistent with results from other studies (Wang et al., 2021; Yuan et al., 2014). This is still a big challenge in accurately estimating GPP.

In general, satellite imagery accurately captures the seasonal leaf phenology of DBF and MF canopies (e.g., spring leaf unfolding and fall senescence). Additionally, the key environmental factors influencing vegetation production during different phenological phases are well-defined (Yuan et al., 2014), making them well-suited for FLAML-LUE modeling. In contrast, the ambiguous seasonal leaf area changes in EBF and the low variability of GPP in NMG ecosystems result in poorer model performance, and empirical methods struggle to estimate GPP variability in these areas (Tramontana et al., 2016).

Model performance is heavily influenced by the quality of the driver data and the typicality of the flux towers. In this study, meteorological indices are obtained directly from spatially explicit reanalysis products. Remotely sensed variables (e.g., NDVI and EVI, LSWI) serve as proxies for vegetation growth and seasonal changes and are crucial for scaling simulations from site to regional levels. These gridded indices are directly derived from satellite reflectance bands. Large-area EFs can be obtained using LE and Hs calculations from ERA5 reanalysis data or can be derived using NDVI temperature triangulation (Venturini et al., 2004). LAI, VPD, Pre, and RH can be obtained from ERA5 reanalysis data. Thus, the model can be extended from the site scale to the regional and even global scale. Building on this foundation, we will develop a long-term gridded GPP dataset for China using the FLAML-LUE framework to analyze its

spatiotemporal variations over multiple years. This dataset will allow us to investigate long-term GPP trends across different climate zones and vegetation types, as well as their responses to key environmental drivers. By comparing GPP estimates across regions and years, we will also assess model uncertainties and identify potential areas for improvement.

5. Conclusion

In this study, the FLAML-LUE model was developed based on data from 20 flux observation sites across China, integrating the FLAML algorithm with key variables from the LUE model. The results demonstrate that the FLAML-LUE model performs excellently in GPP prediction, accurately simulating both its temporal variations and magnitude, particularly in mixed forests and coniferous forests. The average R^2 for daily-scale simulations reached 0.92 and 0.91, respectively. Further analysis showed that extending the temporal scale of input data significantly improves model accuracy. In a comparison of models with different variable combinations, it was found that the model driven by EVI outperformed those driven by NDVI and LAI. The model using LSWI as the driving variable performed better than those with EF, SW, CPD, Pre, and RH as primary variables, with the EVI+LSWI combination yielding the best performance. Additionally, the model's prediction accuracy decreased under high temperature and high VPD conditions. However, under drought conditions, the overall prediction accuracy increased, although it decreased at some sites.

In summary, the FLAML-LUE model demonstrates strong applicability and potential for wider application in GPP estimation. It holds promise for scaling from site-

level to regional or even global levels, contributing to a deeper understanding of carbon

cycling processes. However, the model's applicability in unique ecosystems, such as

alpine shrublands, remains limited, and its ability to adapt to extreme climate events

requires further enhancement. Future work should focus on optimizing the model

structure and parameter settings to improve its robustness and generalization across

diverse ecological environments.

CRediT authorship contribution statement

J.L., Y.Z. and J.W. conceived the study. J.L. collected and processed the data. J.L.

and Y.Z. drafted the manuscript. A.W., Y.Z., R.L and W.D. funded the study. J.L., Y.Z.,

A.W, W.F. and J.W. checked the negatives and touched up. All authors have read and

agreed to the embellished manuscript.

Data availability

A Fast Library for Automated Machine Learning & Tuning (FLAML) is a Python

library, and detailed documentation about FLAML can be found on GitHub. We have

uploaded the related source code and documentation to Zenodo

(https://doi.org/10.5281/zenodo.14874754, Laijie, 2025). The flux observation data and

the Python source code of the FLAML-LUE used in this paper are also archived on

Zenodo (https://doi.org/10.5281/zenodo.15477703, Laijie, 2024).

Declaration of competing interests

The authors declare that they have no known competing financial interests or

personal relationships that could have appeared to influence the work reported in this

paper.

Acknowledgments

This study was financially supported by the National Key Research and Development Program of China (Grant Number: 2022YFF1300501), the Natural Science Foundation of Liaoning Province (Grant Number: 2024-BSBA-62), the Open Research Fund Project of Key Laboratory of Ecosystem Carbon Source and Sink, China Meteorological Administration (Grant Number: ECSS-CMA202305), the Fundamental Research Funds of the Chinese Academy of Meteorological Sciences (Grant Number: 2024Z001). This work utilized eddy covariance data obtained from ChinaFlux. We appreciate all the staff at ChinaFlux for providing high-quality measurement data to the scientific community.

References

Adams, M.D., Massey, F., Chastko, K., Cupini, C., 2020. Spatial modelling of particulate matter air pollution sensor measurements collected by community scientists while cycling, land use regression with spatial cross-validation, and applications of machine learning for data correction. Atmos. Environ. 230, 117479. https://doi.org/10.1016/j.atmosenv.2020.117479

Alemohammad, S.H., Fang, B., Konings, A.G., Aires, F., Green, J.K., Kolassa, J., Miralles, D., Prigent, C., Gentine, P., 2017. Water, Energy, and Carbon with Artificial Neural Networks (WECANN): a statistically based estimate of global surface turbulent fluxes and gross primary productivity using solar-induced fluorescence. Biogeosciences 14, 4101–4124. https://doi.org/10.5194/bg-14-4101-2017

Anderson, G.B., Bell, M.L., 2010. Heat Waves in the United States: Mortality Risk during Heat Waves and Effect Modification by Heat Wave Characteristics in 43 U.S. Communities. Environ. Health Perspect. 119, 210. https://doi.org/10.1289/ehp.1002313

Anderson, M.C., Norman, J.M., Mecikalski, J.R., Otkin, J.A., Kustas, W.P., 2007. A climatological study of evapotranspiration and moisture stress across the continental United States based on thermal remote sensing: 2. Surface moisture climatology. J. Geophys. Res. Atmospheres 112. https://doi.org/10.1029/2006JD007507

Ayantobo, O.O., Li, Y., Song, S., 2019. Multivariate Drought Frequency Analysis using Four-Variate Symmetric and Asymmetric Archimedean Copula Functions. Water Resour. Manag. 33, 103–127. https://doi.org/10.1007/s11269-018-2090-6

Barbour, M.T., 2021. Estimating Organic Carbon Burial in Freshwater Impoundments with a Rapid-Assessment Model and Geospatial Analysis (M.S.).

Beer, C., Reichstein, M., Tomelleri, E., Ciais, P., Jung, M., Carvalhais, N., Rödenbeck, C., Arain,

M.A., Baldocchi, D., Bonan, G.B., Bondeau, A., Cescatti, A., Lasslop, G., Lindroth, A., Lomas, M., Luyssaert, S., Margolis, H., Oleson, K.W., Roupsard, O., Veenendaal, E., Viovy, N., Williams, C., Woodward, F.I., Papale, D., 2010. Terrestrial Gross Carbon Dioxide Uptake: Global Distribution and Covariation with Climate. Science 329, 834–838. https://doi.org/10.1126/science.1184984

Bhattacharyya, P., Neogi, S., Singha Roy, K., Rao, K.S., 2013. Gross primary production, ecosystem respiration and net ecosystem exchange in Asian rice paddy: An eddy covariance-based approach. Curr. Sci. 104, 67–75.

Breiman, L., 2001. Random Forests. Mach. Learn. 45, 5–32. https://doi.org/10.1023/A:1010933404324

Brownlee, J., 2020. Histogram-Based Gradient Boosting Ensembles in Python. MachineLearningMastery.com. URL https://www.machinelearningmastery.com/histogram-based-gradient-boosting-ensembles/ (accessed 5.20.25).

Cai, W., Ullah, S., Yan, L., Lin, Y., 2021. Remote Sensing of Ecosystem Water Use Efficiency: A Review of Direct and Indirect Estimation Methods. Remote Sens. 13, 2393. https://doi.org/10.3390/rs13122393

Cai, W., Yuan, W., Liang, S., Liu, S., Dong, W., Chen, Y., Liu, D., Zhang, H., 2014. Large Differences in Terrestrial Vegetation Production Derived from Satellite-Based Light Use Efficiency Models. Remote Sens. 6, 8945–8965. https://doi.org/10.3390/rs6098945

Chaney, N.W., Herman, J.D., Ek, M.B., Wood, E.F., 2016. Deriving global parameter estimates for the Noah land surface model using FLUXNET and machine learning. J. Geophys. Res. Atmospheres 121, 13,218-13,235. https://doi.org/10.1002/2016JD024821

Chang, X., Xing, Y., Gong, W., Yang, C., Guo, Z., Wang, D., Wang, J., Yang, H., Xue, G., Yang, S., 2023. Evaluating gross primary productivity over 9 ChinaFlux sites based on random forest regression models, remote sensing, and eddy covariance data. Sci. Total Environ. 875, 162601. https://doi.org/10.1016/j.scitotenv.2023.162601

Chen, A., Huang, L., Liu, Q., Piao, S., 2021. Optimal temperature of vegetation productivity and its linkage with climate and elevation on the Tibetan Plateau. Glob. Change Biol. 27, 1942–1951. https://doi.org/10.1111/gcb.15542

Chen, S.-P., Cui-Hai, Y.O.U., Zhong-Min, H.U., Zhi, C., Lei-Ming, Z., Qiu-Feng, W., 2020. Eddy covariance technique and its applications in flux observations of terrestrial ecosystems. Chin. J. Plant Ecol. 44, 291. https://doi.org/10.17521/cjpe.2019.0351

Chen, T., Guestrin, C., 2016. XGBoost: A Scalable Tree Boosting System, in: Proceedings of the 22nd ACM SIGKDD International Conference on Knowledge Discovery and Data Mining, KDD '16. Association for Computing Machinery, New York, NY, USA, pp. 785–794. https://doi.org/10.1145/2939672.2939785

Chen, Y., Feng, X., Fu, B., Wu, X., Gao, Z., 2021. Improved Global Maps of the Optimum Growth Temperature, Maximum Light Use Efficiency, and Gross Primary Production for Vegetation. J. Geophys. Res. Biogeosciences 126, e2020JG005651. https://doi.org/10.1029/2020JG005651

Coops, N.C., Waring, R.H., 2001. The use of multiscale remote sensing imagery to derive regional estimates of forest growth capacity using 3-PGS. Remote Sens. Environ. 75, 324–334. https://doi.org/10.1016/S0034-4257(00)00176-0

980 Cover, T., Hart, P., 1967. Nearest neighbor pattern classification. IEEE Trans. Inf. Theory 13, 21–
981   27. https://doi.org/10.1109/TIT.1967.1053964

982 Cox, P.M., Betts, R.A., Jones, C.D., Spall, S.A., Totterdell, I.J., 2000. Erratum: Acceleration of
983   global warming due to carbon-cycle feedbacks in a coupled climate model. Nature 408,
984   750–750. https://doi.org/10.1038/35047138

985 Ercoli, L., 1993. Relationship between nitrogen and chlorophyll content and spectral properties in
986   maize leaves. Eur. J. Agron.

987 Erickson, N., Mueller, J., Shirkov, A., Zhang, H., Larroy, P., Li, M., Smola, A., 2020. AutoGluon-
988   Tabular: Robust   and   Accurate   AutoML   for   Structured   Data.
989   https://doi.org/10.48550/arXiv.2003.06505

990 Frank, Dorothea, Reichstein, M., Bahn, M., Thonicke, K., Frank, David, Mahecha, M.D., Smith, P.,
991   van der Velde, M., Vicca, S., Babst, F., Beer, C., Buchmann, N., Canadell, J.G., Ciais, P.,
992   Cramer, W., Ibrom, A., Miglietta, F., Poulter, B., Rammig, A., Seneviratne, S.I., Walz, A.,
993   Wattenbach, M., Zavala, M.A., Zscheischler, J., 2015. Effects of climate extremes on the
994   terrestrial carbon cycle: concepts, processes and potential future impacts. Glob. Change
995   Biol. 21, 2861–2880. https://doi.org/10.1111/gcb.12916

996 Geurts, P., Ernst, D., Wehenkel, L., 2006. Extremely randomized trees. Mach. Learn. 63, 3–42.
997   https://doi.org/10.1007/s10994-006-6226-1

998 Gherardi, L.A., Sala, O.E., 2020. Global patterns and climatic controls of belowground net carbon
999   fixation.   Proc.   Natl.   Acad.   Sci.   117,   20038–20043.
1000   https://doi.org/10.1073/pnas.2006715117

1001 Gorelick, N., Hancher, M., Dixon, M., Ilyushchenko, S., Thau, D., Moore, R., 2017. Google Earth
1002   Engine: Planetary-scale geospatial analysis for everyone. Remote Sens. Environ., Big
1003   Remotely   Sensed   Data: tools,   applications   and   experiences   202,   18–27.
1004   https://doi.org/10.1016/j.rse.2017.06.031

1005 Gumus, V., 2023. Evaluating the effect of the SPI and SPEI methods on drought monitoring over
1006   Turkey. J. Hydrol. 626, 130386. https://doi.org/10.1016/j.jhydrol.2023.130386

1007 Guo, Q., Hu, Z., Li, S., Yu, G., Sun, X., Zhang, L., Mu, S., Zhu, X., Wang, Y., Li, Y., Zhao, W., 2015.
1008   Contrasting responses of gross primary productivity to precipitation events in a water-
1009   limited and a temperature-limited grassland ecosystem. Agric. For. Meteorol. 214–215,
1010   169–177. https://doi.org/10.1016/j.agrformet.2015.08.251

1011 Harris, N.L., Gibbs, D.A., Baccini, A., Birdsey, R.A., de Bruin, S., Farina, M., Fatoyinbo, L., Hansen,
1012   M.C., Herold, M., Houghton, R.A., Potapov, P.V., Suarez, D.R., Roman-Cuesta, R.M.,
1013   Saatchi, S.S., Slay, C.M., Turubanova, S.A., Tyukavina, A., 2021. Global maps of twenty-
1014   first   century   forest   carbon   fluxes.   Nat.   Clim.   Change   11,   234–240.
1015   https://doi.org/10.1038/s41558-020-00976-6

1016 He, X., Zhao, K., Chu, X., 2021. AutoML: A survey of the state-of-the-art. Knowl.-Based Syst. 212,
1017   106622. https://doi.org/10.1016/j.knosys.2020.106622

1018 Hersbach, H., Bell, B., Berrisford, P., Hirahara, S., Horányi, A., Muñoz-Sabater, J., Nicolas, J.,
1019   Peubey, C., Radu, R., Schepers, D., Simmons, A., Soci, C., Abdalla, S., Abellan, X.,
1020   Balsamo, G., Bechtold, P., Biavati, G., Bidlot, J., Bonavita, M., De Chiara, G., Dahlgren,
1021   P., Dee, D., Diamantakis, M., Dragani, R., Flemming, J., Forbes, R., Fuentes, M., Geer, A.,
1022   Haimberger, L., Healy, S., Hogan, R.J., Hólm, E., Janisková, M., Keeley, S., Laloyaux, P.,
1023   Lopez, P., Lupu, C., Radnoti, G., de Rosnay, P., Rozum, I., Vamborg, F., Villaume, S.,

Thépaut, J.-N., 2020. The ERA5 global reanalysis. Q. J. R. Meteorol. Soc. 146, 1999–2049. https://doi.org/10.1002/qj.3803

Jiang, G., Sun, R., Zhang, L., Liu, S., Xu, Z., Qiao, C., 2014. Analysis of light use efficiency and gross primary productivity based on remote sensing data over a phragmites-dominated wetland in Zhangye, China, in: Land Surface Remote Sensing II. Presented at the Land Surface Remote Sensing II, SPIE, pp. 571–578. https://doi.org/10.1117/12.2068840

Jung, M., Reichstein, M., Margolis, H.A., Cescatti, A., Richardson, A.D., Arain, M.A., Arneth, A., Bernhofer, C., Bonal, D., Chen, J., Gianelle, D., Gobron, N., Kiely, G., Kutsch, W., Lasslop, G., Law, B.E., Lindroth, A., Merbold, L., Montagnani, L., Moors, E.J., Papale, D., Sottocornola, M., Vaccari, F., Williams, C., 2011. Global patterns of land-atmosphere fluxes of carbon dioxide, latent heat, and sensible heat derived from eddy covariance, satellite, and meteorological observations. J. Geophys. Res. Biogeosciences 116. https://doi.org/10.1029/2010JG001566

Jung, M., Schwalm, C., Migliavacca, M., Walther, S., Camps-Valls, G., Koirala, S., Anthoni, P., Besnard, S., Bodesheim, P., Carvalhais, N., Chevallier, F., Gans, F., Goll, D.S., Haverd, V., Köhler, P., Ichii, K., Jain, A.K., Liu, J., Lombardozzi, D., Nabel, J.E.M.S., Nelson, J.A., O'Sullivan, M., Pallandt, M., Papale, D., Peters, W., Pongratz, J., Rödenbeck, C., Sitch, S., Tramontana, G., Walker, A., Weber, U., Reichstein, M., 2020. Scaling carbon fluxes from eddy covariance sites to globe: synthesis and evaluation of the FLUXCOM approach. Biogeosciences 17, 1343–1365. https://doi.org/10.5194/bg-17-1343-2020

Ke, G., Meng, Q., Finley, T., Wang, T., Chen, W., Ma, W., Ye, Q., Liu, T.-Y., 2017. LightGBM: A Highly Efficient Gradient Boosting Decision Tree, in: Guyon, I., Luxburg, U.V., Bengio, S., Wallach, H., Fergus, R., Vishwanathan, S., Garnett, R. (Eds.), ADVANCES IN NEURAL INFORMATION PROCESSING SYSTEMS 30 (NIPS 2017), Advances in Neural Information Processing Systems. Presented at the 31st Annual Conference on Neural Information Processing Systems (NIPS), Neural Information Processing Systems (nips), La Jolla.

Kong, D., Yuan, D., Li, H., Zhang, J., Yang, S., Li, Y., Bai, Y., Zhang, S., 2023. Improving the Estimation of Gross Primary Productivity across Global Biomes by Modeling Light Use Efficiency through Machine Learning. Remote Sens. 15, 2086. https://doi.org/10.3390/rs15082086

Landry, J.-S., Matthews, H.D., 2016. Non-deforestation fire vs. fossil fuel combustion: The source of CO_2 emissions affects the global carbon cycle and climate responses. Biogeosciences 13, 2137–2149. https://doi.org/10.5194/bg-13-2137-2016

LeDell, E., Poirier, S., 2020. H2O AutoML: Scalable Automatic Machine Learning.

Li, H., Zhang, F., Li, Y., Wang, J., Zhang, L., Zhao, L., Cao, G., Zhao, X., Du, M., 2016. Seasonal and inter-annual variations in CO_2 fluxes over 10 years in an alpine shrubland on the Qinghai-Tibetan Plateau, China. Agric. For. Meteorol. 228–229, 95–103. https://doi.org/10.1016/j.agrformet.2016.06.020

Lloyd, J., Taylor, J.A., 1994. On the Temperature Dependence of Soil Respiration. Funct. Ecol. 8, 315–323. https://doi.org/10.2307/2389824

Mahadevan, P., Wofsy, S.C., Matross, D.M., Xiao, X., Dunn, A.L., Lin, J.C., Gerbig, C., Munger, J.W., Chow, V.Y., Gottlieb, E.W., 2008. A satellite-based biosphere parameterization for net ecosystem CO_2 exchange: Vegetation Photosynthesis and Respiration Model (VPRM).

1068   Glob. Biogeochem. Cycles 22. https://doi.org/10.1029/2006GB002735

1069 McDowell, N., Pockman, W.T., Allen, C.D., Breshears, D.D., Cobb, N., Kolb, T., Plaut, J., Sperry,
1070   J., West, A., Williams, D.G., Yepez, E.A., 2008. Mechanisms of plant survival and mortality
1071   during drought: why do some plants survive while others succumb to drought? New Phytol.
1072   178, 719–739. https://doi.org/10.1111/j.1469-8137.2008.02436.x

1073 Melanie, 2023. TPOT: All about this Machine Learning Python library. Data Sci. Courses
1074   DataScientest. URL https://datascientest.com/en/tpot-all-about-this-machine-learning-
1075   python-library (accessed 6.2.24).

1076 Menefee, D., Lee, T.O., Flynn, K.C., Chen, J., Abraha, M., Baker, J., Suyker, A., 2023. Machine
1077   learning algorithms improve MODIS GPP estimates in United States croplands. Front.
1078   Remote Sens. 4. https://doi.org/10.3389/frsen.2023.1240895

1079 Metin, A., Bilgin, T.T., 2024. Automated machine learning for fabric quality prediction: a
1080   comparative analysis. PeerJ Comput. Sci. 10, e2188. https://doi.org/10.7717/peerj-cs.2188

1081 Nakano, S., Liu, Y., 2025. Interpreting Temporal Shifts in Global Annual Data Using Local
1082   Surrogate Models. Mathematics 13, 626. https://doi.org/10.3390/math13040626

1083 Novick, K.A., Ficklin, D.L., Stoy, P.C., Williams, C.A., Bohrer, G., Oishi, A.C., Papuga, S.A.,
1084   Blanken, P.D., Noormets, A., Sulman, B.N., Scott, R.L., Wang, L., Phillips, R.P., 2016. The
1085   increasing importance of atmospheric demand for ecosystem water and carbon fluxes. Nat.
1086   Clim. Change 6, 1023–1027. https://doi.org/10.1038/nclimate3114

1087 Pagán, B.R., Maes, W.H., Gentine, P., Martens, B., Miralles, D.G., 2019. Exploring the Potential of
1088   Satellite Solar-Induced Fluorescence to Constrain Global Transpiration Estimates. Remote
1089   Sens. 11, 413. https://doi.org/10.3390/rs11040413

1090 Pei, Y., Dong, J., Zhang, Y., Yuan, W., Doughty, R., Yang, J., Zhou, D., Zhang, L., Xiao, X., 2022.
1091   Evolution of light use efficiency models: Improvement, uncertainties, and implications.
1092   Agric. For. Meteorol. 317, 108905. https://doi.org/10.1016/j.agrformet.2022.108905

1093 Peltoniemi, M., Pulkkinen, M., Kolari, P., Duursma, R.A., Montagnani, L., Wharton, S., Lagergren,
1094   F., Takagi, K., Verbeeck, H., Christensen, T., Vesala, T., Falk, M., Loustau, D., Mäkelä, A.,
1095   2012. Does canopy mean nitrogen concentration explain variation in canopy light use
1096   efficiency across 14 contrasting forest sites? Tree Physiol. 32, 200–218.
1097   https://doi.org/10.1093/treephys/tpr140

1098 Potter, C.S., Randerson, J.T., Field, C.B., Matson, P.A., Vitousek, P.M., Mooney, H.A., Klooster,
1099   S.A., 1993. Terrestrial ecosystem production: A process model based on global satellite and
1100   surface data. Glob. Biogeochem. Cycles 7, 811–841. https://doi.org/10.1029/93GB02725

1101 Prokhorenkova, L., Gusev, G., Vorobev, A., Dorogush, A.V., Gulin, A., 2018. CatBoost: unbiased
1102   boosting with categorical features, in: Bengio, S., Wallach, H., Larochelle, H., Grauman,
1103   K., CesaBianchi, N., Garnett, R. (Eds.), ADVANCES IN NEURAL INFORMATION
1104   PROCESSING SYSTEMS 31 (NIPS 2018), Advances in Neural Information Processing
1105   Systems. Presented at the 32nd Conference on Neural Information Processing Systems
1106   (NIPS), Neural Information Processing Systems (nips), La Jolla.

1107 Qian, L., Yu, X., Zhang, Z., Wu, L., Fan, J., Xiang, Y., Chen, J., Liu, X., 2024. Assessing and
1108   improving the high uncertainty of global gross primary productivity products based on deep
1109   learning under extreme climatic conditions. Sci. Total Environ. 957, 177344.
1110   https://doi.org/10.1016/j.scitotenv.2024.177344

1111 Qian, L., Zhang, Z., Wu, L., Fan, S., Yu, X., Liu, X., Ba, Y., Ma, H., Wang, Y., 2023. High uncertainty

1112   of evapotranspiration products under extreme climatic conditions. J. Hydrol. 626, 130332.
1113   https://doi.org/10.1016/j.jhydrol.2023.130332

1114   Qu, L., De Boeck, H.J., Fan, H., Dong, G., Chen, J., Xu, W., Ge, Z., Huang, Z., Shao, C., Hu, Y.,
1115   2020. Diverging Responses of Two Subtropical Tree Species (Schima superba and
1116   Cunninghamia lanceolata) to Heat Waves. Forests 11, 513.
1117   https://doi.org/10.3390/f11050513

1118   Reichstein, M., Bahn, M., Ciais, P., Frank, D., Mahecha, M.D., Seneviratne, S.I., Zscheischler, J.,
1119   Beer, C., Buchmann, N., Frank, D.C., Papale, D., Rammig, A., Smith, P., Thonicke, K., van
1120   der Velde, M., Vicca, S., Walz, A., Wattenbach, M., 2013. Climate extremes and the carbon
1121   cycle. Nature 500, 287–295. https://doi.org/10.1038/nature12350

1122   Reichstein, M., Camps-Valls, G., Stevens, B., Jung, M., Denzler, J., Carvalhais, N., Prabhat, 2019.
1123   Deep learning and process understanding for data-driven Earth system science. Nature 566,
1124   195–204. https://doi.org/10.1038/s41586-019-0912-1

1125   Reichstein, M., Ciais, P., Papale, D., Valentini, R., Running, S., Viovy, N., Cramer, W., Granier, A.,
1126   Ogee, J., Allard, V., Aubinet, M., Bernhofer, C., Buchmann, N., Carrara, A., Grunwald, T.,
1127   Heimann, M., Heinesch, B., Knohl, A., Kutsch, W., Loustau, D., Manca, G., Matteucci, G.,
1128   Miglietta, F., Ourcival, J., Pilegaard, K., Pumpanen, J., Rambal, S., Schaphoff, S., Seufert,
1129   G., Soussana, J.-F., Sanz, M.-J., Vesala, T., Zhao, M., 2007. Reduction of ecosystem
1130   productivity and respiration during the European summer 2003 climate anomaly: a joint
1131   flux tower, remote sensing and modelling analysis. Glob. Change Biol. 13, 634–651.
1132   https://doi.org/10.1111/j.1365-2486.2006.01224.x

1133   Reichstein, M., Falge, E., Baldocchi, D., Papale, D., Aubinet, M., Berbigier, P., Bernhofer, C.,
1134   Buchmann, N., Gilmanov, T., Granier, A., Grünwald, T., Havránková, K., Ilvesniemi, H.,
1135   Janous, D., Knohl, A., Laurila, T., Lohila, A., Loustau, D., Matteucci, G., Meyers, T.,
1136   Miglietta, F., Ourcival, J.-M., Pumpanen, J., Rambal, S., Rotenberg, E., Sanz, M., Tenhunen,
1137   J., Seufert, G., Vaccari, F., Vesala, T., Yakir, D., Valentini, R., 2005. On the separation of
1138   net ecosystem exchange into assimilation and ecosystem respiration: review and improved
1139   algorithm. Glob. Change Biol. 11, 1424–1439. https://doi.org/10.1111/j.1365-
1140   2486.2005.001002.x

1141   Rigden, A.J., Mueller, N.D., Holbrook, N.M., Pillai, N., Huybers, P., 2020. Combined influence of
1142   soil moisture and atmospheric evaporative demand is important for accurately predicting
1143   US maize yields. Nat. Food 1, 127–133. https://doi.org/10.1038/s43016-020-0028-7

1144   Rosebrock, A., 2019. Auto-Keras and AutoML: A Getting Started Guide. PyImageSearch. URL
1145   https://pyimagesearch.com/2019/01/07/auto-keras-and-automl-a-getting-started-guide/
1146   (accessed 6.2.24).

1147   Running, S.W., Nemani, R.R., Heinsch, F.A., Zhao, M., Reeves, M., Hashimoto, H., 2004. A
1148   Continuous Satellite-Derived Measure of Global Terrestrial Primary Production.
1149   BioScience 54, 547–560. https://doi.org/10.1641/0006-
1150   3568(2004)054[0547:ACSMOG]2.0.CO;2

1151   Schmid, H.P., 2002. Footprint modeling for vegetation atmosphere exchange studies: a review and
1152   perspective. Agric. For. Meteorol., FLUXNET 2000 Synthesis 113, 159–183.
1153   https://doi.org/10.1016/S0168-1923(02)00107-7

1154   Sellers, P.J., Schimel, D.S., Moore, B., Liu, J., Eldering, A., 2018. Observing carbon cycle–climate
1155   feedbacks from space. Proc. Natl. Acad. Sci. 115, 7860–7868.

https://doi.org/10.1073/pnas.1716613115

Stefanon, M., D'Andrea, F., Drobinski, P., 2012. Heatwave classification over Europe and the Mediterranean region. Environ. Res. Lett. 7, 014023. https://doi.org/10.1088/1748-9326/7/1/014023

Taylor, K.E., 2001. Summarizing multiple aspects of model performance in a single diagram. J. Geophys. Res. Atmospheres 106, 7183–7192. https://doi.org/10.1029/2000JD900719

Thornton, C., Hutter, F., Hoos, H.H., Leyton-Brown, K., 2013. Auto-WEKA: Combined Selection and Hyperparameter Optimization of Classification Algorithms. https://doi.org/10.48550/arXiv.1208.3719

Tramontana, G., Jung, M., Schwalm, C.R., Ichii, K., Camps-Valls, G., Ráduly, B., Reichstein, M., Arain, M.A., Cescatti, A., Kiely, G., Merbold, L., Serrano-Ortiz, P., Sickert, S., Wolf, S., Papale, D., 2016. Predicting carbon dioxide and energy fluxes across global FLUXNET sites with regression algorithms. Biogeosciences 13, 4291–4313. https://doi.org/10.5194/bg-13-4291-2016

Vaswani, A., Shazeer, N., Parmar, N., Uszkoreit, J., Jones, L., Gomez, A.N., Kaiser, L., Polosukhin, I., 2023. Attention Is All You Need. https://doi.org/10.48550/arXiv.1706.03762

Venturini, V., Bisht, G., Islam, S., Jiang, L., 2004. Comparison of evaporative fractions estimated from AVHRR and MODIS sensors over South Florida. Remote Sens. Environ. 93, 77–86. https://doi.org/10.1016/j.rse.2004.06.020

Vicca, S., Bahn, M., Estiarte, M., van Loon, E.E., Vargas, R., Alberti, G., Ambus, P., Arain, M.A., Beier, C., Bentley, L.P., Borken, W., Buchmann, N., Collins, S.L., de Dato, G., Dukes, J.S., Escolar, C., Fay, P., Guidolotti, G., Hanson, P.J., Kahmen, A., Kröel-Dulay, G., Ladreiter-Knauss, T., Larsen, K.S., Lellei-Kovacs, E., Lebrija-Trejos, E., Maestre, F.T., Marhan, S., Marshall, M., Meir, P., Miao, Y., Muhr, J., Niklaus, P.A., Ogaya, R., Peñuelas, J., Poll, C., Rustad, L.E., Savage, K., Schindlbacher, A., Schmidt, I.K., Smith, A.R., Sotta, E.D., Suseela, V., Tietema, A., van Gestel, N., van Straaten, O., Wan, S., Weber, U., Janssens, I.A., 2014. Can current moisture responses predict soil CO_2 efflux under altered precipitation regimes? A synthesis of manipulation experiments. Biogeosciences 11, 2991–3013. https://doi.org/10.5194/bg-11-2991-2014

Vicente-Serrano, S.M., Beguería, S., López-Moreno, J.I., 2010. A Multiscalar Drought Index Sensitive to Global Warming: The Standardized Precipitation Evapotranspiration Index. https://doi.org/10.1175/2009JCLI2909.1

Wang, C., Wu, Q., Liu, X., Quintanilla, L., 2022. Automated Machine Learning & Tuning with FLAML, in: Proceedings of the 28th ACM SIGKDD Conference on Knowledge Discovery and Data Mining, KDD '22. Association for Computing Machinery, New York, NY, USA, pp. 4828–4829. https://doi.org/10.1145/3534678.3542636

Wang, C., Wu, Q., Weimer, M., Zhu, E., 2021. FLAML: A Fast and Lightweight AutoML Library. https://doi.org/10.48550/arXiv.1911.04706

Wang, H., Guan, H., Liu, B., Chen, X., 2023. Impacts of climate extremes on vegetation dynamics in a transect along the Hu Line of China. Ecol. Indic. 155, 111043. https://doi.org/10.1016/j.ecolind.2023.111043

Wang, H., He, B., Zhang, Y., Huang, L., Chen, Z., Liu, J., 2018. Response of ecosystem productivity to dry/wet conditions indicated by different drought indices. Sci. Total Environ. 612, 347–357. https://doi.org/10.1016/j.scitotenv.2017.08.212

Wang, J., Liu, J., Cao, M., Liu, Y., Yu, G., Li, G., Qi, S., Li, K., 2011. Modelling carbon fluxes of different forests by coupling a remote-sensing model with an ecosystem process model. Int. J. Remote Sens. 32, 6539–6567. https://doi.org/10.1080/01431161.2010.512933

Wang, Y., Li, R., Hu, J., Fu, Y., Duan, J., Cheng, Y., 2021. Daily estimation of gross primary production under all sky using a light use efficiency model coupled with satellite passive microwave measurements. Remote Sens. Environ. 267, 112721. https://doi.org/10.1016/j.rse.2021.112721

Xiao, J., Chevallier, F., Gomez, C., Guanter, L., Hicke, J.A., Huete, A.R., Ichii, K., Ni, W., Pang, Y., Rahman, A.F., Sun, G., Yuan, W., Zhang, L., Zhang, X., 2019. Remote sensing of the terrestrial carbon cycle: A review of advances over 50 years. Remote Sens. Environ. 233, 111383. https://doi.org/10.1016/j.rse.2019.111383

Xiao, X., Braswell, B., Zhang, Q., Boles, S., Frolking, S., Moore, B., 2003. Sensitivity of vegetation indices to atmospheric aerosols: continental-scale observations in Northern Asia. Remote Sens. Environ. 84, 385–392. https://doi.org/10.1016/S0034-4257(02)00129-3

Xiao, X., Hollinger, D., Aber, J., Goltz, M., Davidson, E.A., Zhang, Q., Moore, B., 2004. Satellite-based modeling of gross primary production in an evergreen needleleaf forest. Remote Sens. Environ. 89, 519–534. https://doi.org/10.1016/j.rse.2003.11.008

Xie, M., Ma, X., Wang, Y., Li, C., Shi, H., Yuan, X., Hellwich, O., Chen, C., Zhang, W., Zhang, C., Ling, Q., Gao, R., Zhang, Y., Ochege, F.U., Frankl, A., De Maeyer, P., Buchmann, N., Feigenwinter, I., Olesen, J.E., Juszczak, R., Jacotot, A., Korrensalo, A., Pitacco, A., Varlagin, A., Shekhar, A., Lohila, A., Carrara, A., Brut, A., Kruijt, B., Loubet, B., Heinesch, B., Chojnicki, B., Helfter, C., Vincke, C., Shao, C., Bernhofer, C., Brümmer, C., Wille, C., Tuittila, E.-S., Nemitz, E., Meggio, F., Dong, G., Lanigan, G., Niedrist, G., Wohlfahrt, G., Zhou, G., Goded, I., Gruenwald, T., Olejnik, J., Jansen, J., Neirynck, J., Tuovinen, J.-P., Zhang, J., Klumpp, K., Pilegaard, K., Šigut, L., Klemedtsson, L., Tezza, L., Hörtnagl, L., Urbaniak, M., Roland, M., Schmidt, M., Sutton, M.A., Hehn, M., Saunders, M., Mauder, M., Aurela, M., Korkiakoski, M., Du, M., Vendrame, N., Kowalska, N., Leahy, P.G., Alekseychik, P., Shi, P., Weslien, P., Chen, S., Fares, S., Friborg, T., Tallec, T., Kato, T., Sachs, T., Maximov, T., di Cella, U.M., Moderow, U., Li, Y., He, Y., Kosugi, Y., Luo, G., 2023. Monitoring of carbon-water fluxes at Eurasian meteorological stations using random forest and remote sensing. Sci. Data 10, 587. https://doi.org/10.1038/s41597-023-02473-9

Yi, K., Li, R., Scanlon, T.M., Lerdau, M.T., Berry, J.A., Yang, X., 2024. Impact of atmospheric dryness on solar-induced chlorophyll fluorescence: Tower-based observations at a temperate forest. Remote Sens. Environ. 306, 114106. https://doi.org/10.1016/j.rse.2024.114106

Yu, G., Ren, W., Chen, Z., Zhang, Leiming, Wang, Q., Wen, X., He, N., Zhang, Li, Fang, H., Zhu, X., Gao, Y., Sun, X., 2016. Construction and progress of Chinese terrestrial ecosystem carbon, nitrogen and water fluxes coordinated observation. J. Geogr. Sci. 26, 803–826. https://doi.org/10.1007/s11442-016-1300-5

Yuan, W., Cai, W., Xia, J., Chen, J., Liu, S., Dong, W., Merbold, L., Law, B., Arain, A., Beringer, J., Bernhofer, C., Black, A., Blanken, P.D., Cescatti, A., Chen, Y., Francois, L., Gianelle, D., Janssens, I.A., Jung, M., Kato, T., Kiely, G., Liu, D., Marcolla, B., Montagnani, L., Raschi, A., Roupsard, O., Varlagin, A., Wohlfahrt, G., 2014. Global comparison of light use efficiency models for simulating terrestrial vegetation gross primary production based on

the LaThuile database. Agric. For. Meteorol. 192–193, 108–120. https://doi.org/10.1016/j.agrformet.2014.03.007

Yuan, W., Liu, S., Yu, G., Bonnefond, J.-M., Chen, J., Davis, K., Desai, A.R., Goldstein, A.H., Gianelle, D., Rossi, F., Suyker, A.E., Verma, S.B., 2010. Global estimates of evapotranspiration and gross primary production based on MODIS and global meteorology data. Remote Sens. Environ. 114, 1416–1431. https://doi.org/10.1016/j.rse.2010.01.022

Yuan, W., Liu, S., Zhou, Guangsheng, Zhou, Guoyi, Tieszen, L.L., Baldocchi, D., Bernhofer, C., Gholz, H., Goldstein, A.H., Goulden, M.L., Hollinger, D.Y., Hu, Y., Law, B.E., Stoy, P.C., Vesala, T., Wofsy, S.C., 2007. Deriving a light use efficiency model from eddy covariance flux data for predicting daily gross primary production across biomes. Agric. For. Meteorol. 143, 189–207. https://doi.org/10.1016/j.agrformet.2006.12.001

Zhang, C., Tian, X., Zhao, Y., Lu, J., 2023. Automated machine learning-based building energy load prediction method. J. Build. Eng. 80, 108071. https://doi.org/10.1016/j.jobe.2023.108071

Zhang, W.L., Chen, S.P., Chen, J., Wei, L., Han, X.G., Lin, G.H., 2007. Biophysical regulations of carbon fluxes of a steppe and a cultivated cropland in semiarid Inner Mongolia. Agric. For. Meteorol. 146, 216–229. https://doi.org/10.1016/j.agrformet.2007.06.002

Zhang, Y., Song, C., Sun, G., Band, L.E., Noormets, A., Zhang, Q., 2015. Understanding moisture stress on light use efficiency across terrestrial ecosystems based on global flux and remote-sensing data. J. Geophys. Res. Biogeosciences 120, 2053–2066. https://doi.org/10.1002/2015JG003023

Zhang, Z., Guo, J., Jin, S., Han, S., 2023. Improving the ability of PRI in light use efficiency estimation by distinguishing sunlit and shaded leaves in rice canopy. Int. J. Remote Sens. 44, 5755–5767. https://doi.org/10.1080/01431161.2023.2252165

Zhao, W.L., Gentine, P., Reichstein, M., Zhang, Y., Zhou, S., Wen, Y., Lin, C., Li, X., Qiu, G.Y., 2019. Physics-Constrained Machine Learning of Evapotranspiration. Geophys. Res. Lett. 46, 14496–14507. https://doi.org/10.1029/2019GL085291

Zheng, Z., Fiore, A.M., Westervelt, D.M., Milly, G.P., Goldsmith, J., Karambelas, A., Curci, G., Randles, C.A., Paiva, A.R., Wang, C., Wu, Q., Dey, S., 2023. Automated Machine Learning to Evaluate the Information Content of Tropospheric Trace Gas Columns for Fine Particle Estimates Over India: A Modeling Testbed. J. Adv. Model. Earth Syst. 15, e2022MS003099. https://doi.org/10.1029/2022MS003099

Zhou, S.-X., Prentice, I.C., Medlyn, B.E., 2019. Bridging Drought Experiment and Modeling: Representing the Differential Sensitivities of Leaf Gas Exchange to Drought. Front. Plant Sci. 9. https://doi.org/10.3389/fpls.2018.01965